THERMO-FLUID MODEL OF MENISCUS BEHAVIOR AND OSCILLATION MARK FORMATION IN STEEL CONTINUOUS CASTING

BY

XIAOLU YAN

THESIS

Submitted in partial fulfillment of the requirements
for the degree of Master of Science in Mechanical Engineering
in the Graduate College of the
University of Illinois at Urbana-Champaign, 2017

Urbana, Illinois

Adviser:

Professor Brian G. Thomas

ABSTRACT

The surface quality of steel depends on initial solidification at the meniscus during continuous casting. A computational thermal-fluid model has been developed to simulate the complex transient behavior of the slag layer between the oscillating mold wall, the slag rim, the slag/liquid steel interface, and the solidifying steel shell in the meniscus region. It includes transient heat transfer, multi-phase fluid flow, solidification of the slag and steel, and movement of the mold during several oscillation cycles. The model is validated with transient temperature measurements and shell strand measurements from a "mold simulator" lab experiment and with plant measurements of oscillation mark (OM) depth and slag consumption. Hook type oscillation mark is predicted to form by steel overflowing the meniscus. In addition to the commonly predicted/measured temperature increase during the negative strip time (NST), a smaller temperature increase is predicted during the positive strip time (PST) for thermocouples near steel level, and can be associated with the overflow event. These discoveries help to explain the overflow mechanism in detail and reveal new insights into the phenomena which govern initial solidification, oscillation mark formation, and surface defects in this process.

ACKNOWLEDGEMENTS

My sincere gratitude to my adviser, Professor Brain G. Thomas, for his continuous support, expertise, guidance and encouragement during this work. I would like to acknowledge the work of previous student A. S. M. Jonayat for early works on this topic. The financial support for this project is provided by the members of Continuous Casting Consortium at University of Illinois at Urbana-Champaign (UIUC), for which I am very grateful.

I would also like to thank my colleagues at Metals Processing Simulation Laboratory Rui Liu, Kai Jin, Lance Hibbeler, Seong-Mook Cho and Hyunjin Yang for their suggestions and insights which have helped me in many occasions. I thank all of my lab mates –Kun Xu, Mathew Zappulla, Prathiba Duvvuri, Zhelin Chen, Nathan Seymour and Adnan Akhtar for making my time in this lab memorable.

Finally, I thank my wife Sushuang Ma for her support during the composition of this manuscript, and my unborn child for the joy and surprise she brings.

TABLE OF CONTENTS

LIST OF FIGURES

LIST OF TABLES

LIST OF SYMBOLS

A_{mush}	Mushy zone parameter
$C_{0,i}$	Initial composition of each alloy components
$C_{L,i}$	Concentration of each solute elements at the interface in the liquid
C_p	Specific heat
D	Cooling water channel diameter
d	Effective mold thickness
d_g	Slag gap thickness during model initialization
d_{TC}	Effect thermocouple depth from mold hot face
F_1	Blending function in $k-\omega$ SST model
$\boldsymbol{F_\sigma}$	Surface tension force at the steel/slag interface
f	Mold oscillation frequency
f_s	Solid phase fraction
$\boldsymbol{g}$	Gravitational accerlation
H_{mix}	Total enthalpy of steel-slag mixture
h_c	Effective convection heat-transfer coefficient at mold cold face
h_{mix}	Sensible enthalpy of steel-slag mixture
h_w	Convection heat-transfer coefficient at water channel surface in ROM model

K	Thermal conductivity
K_{eff}	Effective thermal conductivity
K_{Cu}	Copper mold thermal conductivity
K_{sol}	Steel shell solidification factor
k	Turbulent energy
k_i	Equilibrium partition coefficient for each alloy component
$k^{\delta/L}$	Equilibrium partition coefficient for δ - ferrite
L	Cooling water channel length
L_{st}	Latent heat of steel
m_i	Slope of liquidus line of each solute element in pseudo-binary Fe-phase diagram
$\widehat{\boldsymbol{n}}$	Unit normal of the surface
$\widehat{\boldsymbol{n}}_{wall}$	Unit normal to wall at three-phase contact line point
$\widehat{\boldsymbol{n}}_t$	Unit normal to interface at three-phase contact point
Pr	Prandtl number
p	Pressure
p_i	Constant pressure at domain top slag inlet
p_o	Constant pressure at domain bottom outlet
Q	Constant uniform heat flux at mold hot face in the 2D ROM model

q_c	Mold cold face heat flux
Re	Reynolds number
$\boldsymbol{S}_{mush}$	Momentum sink
s	Mold oscillation stroke
S	Steel shell thickness
T	Temperature
T_a	Constant temperature at domain top slag inlet
T_b	Back flow temperature at domain bottom outlet
T_c	Mold cold face temperature in ROM model
T_h	Mold hot face temperature in ROM model
T_i	Constant temperature at steel inlet
T_{liq}	Liquidus temperature of steel
T_{pure}	Melting point of pure iron
T_{ref}	Arbitrary reference temperature for enthalpy calculation
T_{sol}	Solidus temperature of steel
T_{TC}	Thermocouple temperature in ROM model
T_w	Mold cooling water temperature
t	Time
t_0	Time in simulation when mold start to oscillate

$\boldsymbol{v}$	Velocity vector
$\boldsymbol{v}_c$	Casting speed
v_m	Instantaneous oscillation velocity of mold
v_x	x direction velocity component
v_y	y direction velocity component
x	Horizontal direction in model domain (from mold wall)
y	Vertical direction in model domain
z	Horizontal direction in model domain (along mold wall)
Y_D	Domain height
Y_{Fe}	Far-field steel surface level
Y_{fix}	Vertical location threshold for velocity fix boundary condition
Y_S	Distance along the shell strand at 17.69s (simulation time)α_{Fe}

Volume fraction of steel phase

α_{sl}	Volume fraction of slag phase
β	Liquid phase fraction
β_{Fe}	Liquid steel phase fraction
$\beta^*, \beta^{'}, \gamma$	Constants in $k-\omega$ SST model
$\bar{\epsilon}$	Von-Mises inelastic strain
$\dot{\bar{\epsilon}}$	Von-Mises inelastic strain rate

$\dot{\epsilon}_{xy}$	Equivalent inelastic strain rate in pure shear condition
$\bar{\sigma}$	Von-Mises stress
σ_{sl-st}	Surface tension at interface between steel/slag
σ_k, σ_ω	constants in $k-\omega$ SST model
τ_{xy}	Equivalent shear stress in pure shear condition
κ	Local curvature of steel/slag interface
ω	Specific dissipation rate
ρ	Density
ρ_{sl}	Density of slag
ρ_{st}	Density of steel
ρ_{mix}	Density of steel-slag mixture
θ_{eq}	Static contact angle at rest/equilibrium between phases
ΔH	Latent heat content
μ	Dynamic viscosity
μ_{st}	Effective viscosity of steel
μ_t	Turbulent dynamic viscosity
μ_{mix}	Mixture dynamic viscosity
ν	Kinematic viscosity

ν_t	Turbulent kinematic viscosity
$\gamma_{Fe(l)-sl}$	Surface tension between liquid steel and slag

CHAPTER 1: INTRODUCTION

Surface defects in continuous casting of steel slabs such as oscillation marks (OMs) and hooks are of particular interest to the industry as they are time consuming and expensive to remove, and they lower the final yield. Oscillation marks (shown in Figure 1.1[1]] on the left) are periodic transverse depressions caused by mold oscillation during initial solidification, and is a common site for crack formation later on. A hook is a microstructural feature that often co-exists with oscillation marks; it extends from the root of OM into the slab, with a curved shape. The shape[2] of etched hooks and the fact that they often come with entrapped slag suggest that hooks form from freezing the meniscus[2]. Hence, to understand the mechanism of hook and OM formation, it is natural to investigate the flow and thermal behavior of the meniscus region during initial solidification.

Figure 1.1(on the right) shows a schematic of the continuous casting process. Molten steel enters the mold through the bifurcated ports of a submerged entry nozzle and flows toward the narrow faces of the mold. The molten steel jets eventually impinge onto the solidified shell at the narrow faces and split into a downward main flow and a secondary upward flow. A tertiary flow/eddy can be induced in the meniscus region by the secondary flow. Surface waves and level fluctuations of the interface of the top free surface of the molten steel surface with the liquid slag can also be induced by the upward secondary flow as it hits the top free surface, due to its chaotic turbulent nature. The meniscus is the part of steel-slag interface that extends above the shell tip, owing to surface tension. The region around the meniscus involves complex flow and thermal phenomena that are interdependent as shown in the schematic in Figure 1.1 at middle. Cooling water goes through grooves inside the mold and extract heat from the steel melt through the steel shell and slag gap. The mold oscillates up and down periodically to prevent the steel shell from sticking. Slag powder is

added to the top surface to provide insulation and lubrication. Slag powder sinters and melts as it move downward, and is finally consumed into the slag gap between the mold the steel shell. Liquid slag will re-solidify against the mold both inside the gap and above the gap, it forms a solid slag rim above the meniscus and oscillates with the mold. The slag rim pulls and pushes on the meniscus as it moves up or down and induces a periodic movement in the steel melt near meniscus. Steel overflow could happen if the meniscus is pulled or pushed too much, and the shell tip is not able to hold in the liquid steel, and this phenomenon is an important aspect of several of the mechanisms[2] for oscillation mark formation.

The scope of this work is to develop a computational model that couples all the meniscus phenomena, including fluid flow, heat transfer, solidification and mold oscillation. Through the use of temperature dependent material property and a set of casting parameters identical to a lab experiment[3] for validation, the model aims to predict transient flow and temperature field near meniscus, steel shell and slag gap profile and most importantly, the formation mechanism of oscillation marks during initial solidification.

1.1 Figure

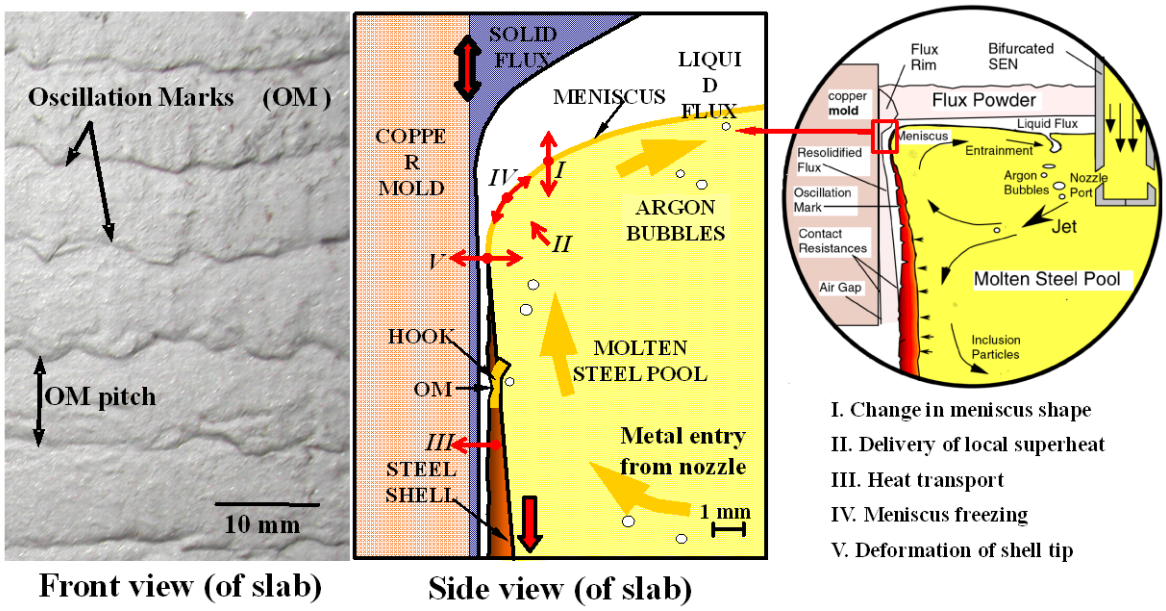

Figure 1.1: Oscillation mark on slab surface and schematic of meniscus phenomena[1]

CHAPTER 2: LITERATURE REVIEW

In order to understand the various phenomena in the meniscus region, many researchers have conducted measurements of the commercial process of continuous casting of steel, including slag consumption, [4][5][6][7] OM depth,[4][8][9][10] and hook depth[11][12]. Sengupta et al measured hook shape and compared it to the theoretical static shape[13] of meniscus and concluded that hook is formed by frozen meniscus. Badri et al[14][15] and Zhang et al[3] investigated initial solidification by experimenting with laboratory-scale mold simulators. An oscillating mold is dipped into a steel melt bath, shell is drawn down relative to the mold by a 3 sided extractor that surrounds the mold. The strand shape and gap were measured after mold was pulled out of the steel melt, and temperature inside the mold was recorded by imbedded thermocouples. Both authors observed a temperature increase/heat flux peak during the negative strip time (NST) near steel level. Oscillation marks on the resultant shell were correlated to the heat flux peak during NST; however, the method for mapping location on the shell strand to a specific time is not mentioned. Based on the correlation of heat flux peak and OM, Badri suggested that OM is formed during the NST due to the meniscus getting close to the mold and rapidly solidifies, which is companied by the observed heat flux peak.

E. Takeuchi and J.K. Brimacombe[16] tried to theorize the OM formation mechanism by combining metallurgical observation and semi-analytical models. Dentrites were found to first grow perpendicular to subsurface hooks or the curved surface of the OM, and latter change orientation to be perpendicular to mold wall. This suggests a relationship between frozen meniscus and OM. Pressure fluctuation in the slag caused by the oscillating mold is determined to be a major factor in OM formation. It was theorized that positive pressure in the negative strip time pushes meniscus away from mold wall, and later on, negative

pressure during the positive strip time (PST) either bends the shell or causes overflow depending on the rigidity of the shell tip.

Many computational models have been developed to investigate some of the important phenomena at the meniscus. These include computational fluid flow models of the turbulent flow[17]-[20], the thermal-flow in the top surface powder layer[21], heat transfer models of the solidifying steel shell, and thermal-flow behavior in the interfacial gap between the mold and shell[22]-[24], and heat transfer models of the mold[25][26].

Sengupta et al[27] investigated shell tip deflection during a steel level fluctuation using a two dimensional (2D) transient thermal-mechanical model (CON2D[28]). This model incorporates temperature dependent properties, thermal shrinkage, phase transformations, and different elastic-viscoplastic constitutive equations for each phase. In their model, Kozlowski's constitutive model III[29] is used for austenite and the modified power law of Zhu[30] is used for delta-ferrite. The shell tip is predicted to deflect away from the mold due to thermal stress after steel level rises following a previous level drop. The predicted shell surface shape resembles the lower portion of many hook measurements. Parametric studies with different steel grades revealed that peritectic and ultra-low-carbon (ULC) steel shells deflect much more during level fluctuations, compared with low or high-carbon steels. This matches the well-known plant observations of the variation of oscillation mark depth with steel grade. It was concluded that the formation of shallow, sub-surface straight hooks and the shape of the lower side of oscillation marks is governed by thermal distortion, which is greatly aggravated by level fluctuations.

Steinruck and Rudischer[31] developed a 2D transient thermal-flow model that includes the steel melt, an elasto-viscoplastic strand shell, slag in the gap between shell and mold. Slag in the gap is modelled by the lubrication theory, while the steel and slag phase interface above

shell tip is fixed to a static shape solved analytically[13]. Temperature dependent steel elastic modulus is used for the shell while all other material property used are constants. Steel in mushy zone is treated as fluid with high viscosity. This model is able to predict OM formation in line with the bending theory: the shell bends away from the mold during NST, and is then pushed back at the start of PST, forming the OM. The new shell forms abruptly during the latter part of PST after the shell tip bent back and meniscus is pushed close to the mold. Parametric study with this model found a positive correlation between average OM depth and slag consumption, suggesting that slag trapped in the oscillation accounts for a major part of the slag consumption. Slag consumption is found to decrease with increasing casting speed, which agrees with previous measurements[4][5][6][7] .

A 2D transient thermal-flow model that focuses on the meniscus region was developed by Ojeda et al.[32][33] and improved by Jonayat et al.[34] This model includes the top slag layer, slag rim, liquid steel, slag gap and the mold in the meniscus region and extends 100mm below the steel level. Steel and slag are separated as two distinct phases and the phase interface shape is calculated by the VOF[35] model. Temperature-dependent slag properties were used following McDavid and Thomas[21]. The meniscus is predicted to flatten due to positive pressure during negative strip time and bulges due to negative pressure during PST. This agrees with lab experiments using mercury or water with silicon oil[36][37]. Thermocouple temperature near the meniscus is predicted to increase during NST as reported by Badri et al[14][15] in a laboratory-based mold simulator. However, this temperature increase/heat flux peak happens when the meniscus is predicted to flatten as opposed to Badri's theory. Predicted slag consumption matches plant measurements by Shin et al. [4] Parametric study using this model shows a decreased slag mass consumption per strand area with increasing casting speed, and increased slag consumption with

increasing oscillation frequency and modification ratio, which agrees with previous measurements[4][5][6][7]. However, solidification of the steel shell is not modelled, as a fixed steel shell shape is instead set as the domain boundary. Hence the model lacks the ability of predicting slag gap thickness, shell thickness and oscillation marks.

Lopez et al.[38][39][40] developed a 2D transient model that couples fluid flow, heat transfer and solidification in a half caster (symmetrical) domain that extend 1.4m below the mold top. This model is able to predict steel solidification using the enthalpy-porosity[41] method, while steel and slag interface is also tracked using the VOF[35] model. Fluid flow in the meniscus region predicted by this model agrees qualitatively with Ojeda[33] and Jonayat[34]. Shell thickness predicted at location 45 mm below meniscus agrees with plant measurements taken by Hanao et al[42], and the general shape of the heat flux variation during an oscillation cycle agrees with the measurements by Badri et al[14][15]. The predicted oscillation mark pitch matches the theoretical value (casting speed/oscillation frequency), and significantly, also produces variations, which are always observed in measurements. However, the oscillation mark depth is predicted to be only 0.04 to 0.1mm, while typical OM depth ranges from 0.2mm to 0.6 in plant and laboratory measurements[3][4][16][43]. Perhaps this is due to insufficient refinement; even though the smallest cell size was 100 μm, the mesh in the critical gap region was more coarse. Also, the presence of meniscus freezing and the lack of overflow predicted by this model suggests that the shell could bend, likely because the viscosity of the solid steel was too low, and the enthalpy-porosity method alone was not able to produce a sufficiently rigid shell to accurately model shell tip behavior.

Previous numerical models have helped to gain understanding of meniscus thermal/flow behaviors, and shed light on the oscillation mark formation mechanisms. However, no model yet is able to reproduce the overflow mechanism for oscillation mark formation and

quantitatively predict OM depth that is reasonably accurate. The current work presents a model that couples fluid flow, heat transfer and solidification in the meniscus region with a high-resolution computational mesh. The model predictions are compared with lab experiment measurements, and the simulations are applied to gain new insight into initial solidification, including the formation of oscillation marks.

CHAPTER 3: COMPUTATIONAL MODEL DEVELOPMENT

3.1 Domain

Figure 3.1 shows the domain of the main model developed in this work. It represents a 2D slice of the continuous-casting process near the meniscus. The domain consists of two sub-domains: the fluid and the mold.

The fluid domain contains slag powder, molten slag, the solidifiying steel shell and molten steel in the meniscus region, that extends 100mm (width) from the mold wall with a length of 150mm, from 100mm below to 50mm above the tip of the solidifying steel shell (length). Steel flow is introduced into the domain on the side opposite to the mold wall near the slag-steel interface, representing a tertiary flow induced by the flow coming from the nozzle. Slag, the solidifying steel shell and some molten steel are able to exit the domain at the bottom near the mold wall.

The solid domain contains the top of the copper mold adjacent to the fluid domain with an effective width of 12.327mm. This effective width is calculated from a 2D heat transfer model that simulates the mold geometry used in Zhang's experiment[3]. Details of this 2D mold heat transfer model will be elaborated in section3.4. The solid domain measures 170mm in length, providing 10mm of extra coverage on beyond the top and bottom of the fluid domain, in order to maintain contact during between the two domains at all times during mold oscillation. Only the heat conduction equation is solved in the solid domain and the two domains are coupled by heat transfer across the vertically moving interface, which represents the contact surface between the mold wall and the solid slag at the edge of the fluid.

3.2 Governing Equations

A transient, 2D, two-phase (slag-steel) thermo-fluid flow-solidification calculation is carried out in the fluid domain as described in Section 3.1. A single set of momentum, continuity, and energy equations are solved on a fixed grid using the volume-of-fluid method[35] (VOF) to determine the slag and steel phase boundaries in the domain.

Slag and steel are modelled as two immiscible phases of the VOF model. They occupy the domain and their volume fractions sum to unity

$$\alpha_{Fe} + \alpha_{sl} = 1 \qquad (3.1)$$

The steel phase fraction is advected by the flow according to the following conservation equation,

$$\frac{\partial \alpha_{Fe}}{\partial t} + \boldsymbol{v} \cdot \nabla \alpha_{Fe} = 0 \qquad (3.2)$$

Where $\boldsymbol{v}$ is the vector of velocity components in the horizontal direction normal to the mold wall (x) and in the vertical casting direction (y).

Material properties (density, viscosity, and thermal conductivity) at each point of the domain are evaluated by mixture equations of α_{Fe} and α_{sl}, such as Eqn. (*3.3* for density of the fluid (ρ_{mix})

$$\rho_{mix} = \alpha_{Fe}\rho_{Fe} + (1 - \alpha_{Fe})\rho_{sl} \qquad (3.3)$$

where ρ_{Fe} and ρ_{sl} are constant densities of steel and slag. Continuity is satisfied by the following overall mass conservation equation:

$$\frac{\partial \rho_{mix}}{\partial t} + \nabla \cdot (\rho_{mix}\boldsymbol{v}) = 0 \qquad (3.4)$$

For momentum conservation, a single set of Navier-Stokes equations given by Eqn. （*3.5* is solved.

$$\rho_{mix}\frac{\partial \boldsymbol{v}}{\partial t}+\rho_{mix}\boldsymbol{v}\cdot\nabla\boldsymbol{v}=-\nabla p+\nabla\cdot[\mu_{mix}(\nabla\boldsymbol{v}+\nabla^{T}\boldsymbol{v})]+\rho_{mix}\boldsymbol{g}+\boldsymbol{F_{\sigma}}-\boldsymbol{S}_{mush} \qquad (3.5)$$

where $\boldsymbol{F_{\sigma}}$ is the momentum source term for the force per unit volume due to surface tension given by the following equation, which is the CSF model of Brackbill et al.[44]

$$\boldsymbol{F_{\sigma}}=\sigma_{sl-Fe}\frac{\rho_{mix}\kappa\nabla\alpha_{sl}}{\frac{1}{2}(\rho_{Fe}+\rho_{sl})} \qquad (3.6)$$

Here, σ_{sl-st} is the constant surface tension of the interface between the slag and steel (N/m), and κ is the local curvature of this interface, found from

$$\kappa=\nabla\cdot\hat{\boldsymbol{n}} \qquad (3.7)$$

Where $\hat{\boldsymbol{n}}$ is the unit normal ($\hat{\boldsymbol{n}}=\boldsymbol{n}/|\boldsymbol{n}|$) of the surface, found from the phase fraction marker field, $\boldsymbol{n}=\nabla\alpha_{sl}$. At the wall boundary, $\hat{\boldsymbol{n}}$ is found from

$$\hat{\boldsymbol{n}}=\hat{\boldsymbol{n}}_{wall}\cos\theta_{eq}+\hat{\boldsymbol{n}}_{t}\sin\theta_{eq} \qquad (3.8)$$

where $\hat{\boldsymbol{n}}_{t}$ is normal to the interface where it contacts the wall and $\hat{\boldsymbol{n}}_{wall}$ is normal to the wall. The angle, θ_{eq}, is the static contact angle when the fluid is at rest. The angle may change (dynamic contact angle, θ_{d}) with interface motion. Without measurements to establish a constitutive law for θ_{d}, θ_{eq} is used in practice.[45]

$\boldsymbol{S}_{mush}$ in Eqn. （*3.5* is a momentum sink term[41] added to simulate the loss of momentum due to the low porosity of the mushy region. The mushy zone is represented by a region with liquid fraction β between 0 and 1. It is modelled as a porous medium with porosity set proportional to a function of the liquid fraction β.

$$\boldsymbol{S}_{mush} = \frac{(1-\beta)^2}{(\beta^3+\varepsilon)^2} A_{mush}(\boldsymbol{v} - \boldsymbol{v}_c) \quad (3.9)$$

Where ε=0.001, $\boldsymbol{v}_c$ is the casting speed, A_{mush} is the mushy zone parameter. The value of the mushy zone parameter is set to vary both with location and time. To represent the cold, rigid structure of the solidified steel shell, A_{mush}=10^7 if the cell is located to the left of x=1mm or below y=Y_{fix} (where Y_{fix} is a time dependent function given in Figure 3.2). To represent the dendrites and interdendritic liquid steel, A_{mush}=10^4 if the cell is located to the right of x=5mm or above y=$Y_{fix}+3$. In between (1mm, Y_{fix}) and (5mm, $Y_{fix}+3$), A_{mush} is set to vary linearly in Logarithmic scale.

The liquid fraction, β used in Eqn. (*3.9*) is for the steel-slag mixture and can be calculated from the liquid fraction of each phase based on their phase fractions. Since slag is treated as 100% liquid in the model, the mixture liquid fraction is only dependent on the steel phase:

$$\beta = \alpha_{Fe}\beta_{Fe} + \alpha_{sl} \times 1 = \alpha_{Fe}\beta_{Fe} + (1 - \alpha_{Fe}) \quad (3.10)$$

where the liquid fraction of steel , β_{Fe} is defined as

$$\begin{cases} \beta_{Fe} = 0 & if\ T < T_{sol} \\ \beta_{Fe} = 1 & if\ T > T_{liq} \\ \beta_{Fe} = \dfrac{T - T_{sol}}{T_{liq} - T_{sol}} & if\ T_{sol} < T < T_{liq} \end{cases} \quad (3.11)$$

Temperature in both the fluid (slag-steel) and solid (mold) regions of the domain is found by first solving the following enthalpy formulation of the energy equation.

$$\frac{\partial}{\partial t}(\rho_{mix} H_{mix}) + \nabla \cdot (\rho_{mix} \boldsymbol{v} H_{mix}) = \nabla \cdot \left(K_{eff} \nabla T\right) \quad (3.12)$$

where the total enthalpy, H_{mix} is computed as the sum of sensible enthalpy, h_{mix}, and latent heat content, ΔH_{mix}

$$H_{mix} = h_{mix} + \Delta H_{mix} \quad (3.13)$$

Assuming a fixed relationship between latent heat evolution, phase fractions, and temperature, the temperature T is found from the enthalpy of the slag-steel mixture, H_{mix}, via eqn. (*3.14*) through (*3.16*)

$$\begin{cases} h_{Fe} = \int_{T_{ref}}^{T} (C_p)_{Fe}\, dT \\ h_{sl} = \int_{T_{ref}}^{T} (C_p)_{sl}\, dT \end{cases} \quad (3.14)$$

where C_p is specific heat, and T_{ref} is an arbitrary reference temperature. For the VOF model, h_{mix} is a mass weighted average over the phase fractions of the slag and steel,

$$h_{mix} = \frac{(\alpha\rho h)_{sl} + (\alpha\rho h)_{Fe}}{(\alpha\rho)_{sl} + (\alpha\rho)_{Fe}} \quad (3.15)$$

Latent heat content of the mixture is also treated as a mass weighted average of slag and steel. However, as solidification of slag is only modeled through temperature-dependent viscosity, the latent heat content of the mixture takes the following form,

$$\Delta H_{mix} = \frac{(\alpha\rho\Delta H)_{Fe}}{(\alpha\rho)_{sl} + (\alpha\rho)_{Fe}} \quad (3.16)$$

where the latent heat content at any location in the domain is calculated as a product of the latent heat of transformation of liquid steel into solid, L_{Fe}, and the liquid fraction of steel, β_{Fe}.

$$\Delta H_{Fe} = \beta_{Fe} L_{Fe} \quad (3.17)$$

Thermal conductivity of the fluid, K_{eff} is the sum of the conductivity of the slag / steel mixture (K_{mix}) and the conductivity due to turbulence (K_t). For turbulence closure,

Menter's[46][47] $k-\omega$ SST model is used. Following the $k-\omega$ SST formulation, two more transport equations are solved for turbulent energy (k) and specific dissipation rate (ω),

$$\frac{\partial}{\partial t}(\rho_{mix}k)+\nabla\cdot(\rho_{mix}k\boldsymbol{v})=\nabla\cdot[(\mu_{mix}+\sigma_k\mu_t)\nabla k]-\beta^*\rho_{mix}\omega k+\tilde{P}_k$$

$$\frac{\partial}{\partial t}(\rho_{mix}\omega)+\nabla\cdot(\rho_{mix}\omega\boldsymbol{v})=\nabla\cdot[(\mu_{mix}+\sigma_\omega\mu_t)\nabla\omega]-\beta'\rho_{mix}\omega^2+\frac{\gamma}{\nu_t}\tilde{P}_k \qquad (3.18)$$

$$+2(1-F_1)\rho_{mix}\sigma_{\omega2}\frac{1}{\omega}\frac{\partial k}{\partial x_j}\frac{\partial\omega}{\partial x_j}$$

Where the production term $\tilde{P}_k$, is

$$\tilde{P}_k=min\left(\mu_t\frac{\partial v_i}{\partial x_j}\left(\frac{\partial v_i}{\partial x_j}+\frac{\partial v_j}{\partial x_i}\right);10\beta^*\rho k\omega\right) \qquad (3.19)$$

The other terms are given by

$$F_1=\tanh\left(\left[min\left\{max\left(\frac{\sqrt{k}}{0.09\omega l};\frac{500\nu}{l^2\omega}\right),\frac{4\rho_{mix}\sigma_{\omega2}k}{CD_{k\omega}l^2}\right\}\right]^4\right) \qquad (3.20)$$

Where,

$$CD_{k\omega}=max\left(2\rho_{mix}\sigma_{\omega2}\frac{1}{\omega}\frac{\partial k}{\partial x_j}\frac{\partial\omega}{\partial x_j},10^{-10}\right) \qquad (3.21)$$

and

$$\nu_t=\frac{\mu_t}{\rho_{mix}}=\frac{a_1k}{max(a_1\omega;|\boldsymbol{S}|F_2)};\quad F_2=\tanh\left(\left\{max\left(2\frac{\sqrt{k}}{0.09\omega l};\frac{500\nu}{l^2\omega}\right)\right\}^2\right) \qquad (3.22)$$

Here l is the distance to the closest wall node, $\boldsymbol{S}$ is the strain rate tensor, $a_1=0.31$, $\beta^*=0.09$, and constants $\beta',\sigma_k,\sigma_\omega,\gamma$ are each found using a weighted average based on the blending fraction, F_1. For example:

$$\beta'=F_1\beta'_1+(1-F_1)\beta'_2 \qquad (3.23)$$

Similar relations are used to find $\sigma_k, \sigma_\omega, \gamma$ where $\sigma_{k1} = 0.85, \sigma_{k2} = 1.0, \sigma_{\omega1} = 0.5, \sigma_{\omega2} = 0.856, \beta'_1 = 0.075, \beta'_2 = 0.0828, \gamma_1 = \frac{5}{9}$, and $\gamma_2 = 0.44$.

F_1 is the blending function and $F_1 = 1$ in the near-wall region (activates $k - \omega$) and $F_1 = 0$ in the outer region (activates $k - \epsilon$).

3.3 Boundary conditions

Boundary conditions on the domains in Fig. 3.1 are described in this section. Values of the parameters used in boundary conditions can be found in table Table 3.1.

3.3.1 Slag top surface

This "pressure inlet" [48] boundary is given a constant ambient pressure, p_i, of 1 atm, with the inflow direction set normal to the surface. Temperature is set to constant T_a as can be found in Table 3.1

3.3.2 Steel inlet

This is a "mass-flow rate" [48] boundary at the vertical right side of the fluid domain, ranging from y=65mm to 92mm. It is set to have the same mass flow rate of steel as the "slag & steel outlet", so as to keep a constant steel level. Velocity is set to be normal to the surface and temperature is set as constant T_i, representing a super heat of 10°C to prevent the whole domain from freezing.

3.3.3 Slag & steel outlet

This is a "constant pressure" boundary that extends from x=0mm to x=65mm. Pressure is set to p_o to represent the ferrostatic pressure at the outlet,

$$p_o = \rho_{Fe} g Y_{Fe} + \rho_{Sl} g (Y_D - Y_{Fe}) \qquad (3.24)$$

where g is the gravitational acceleration, (9.8 m/s^2), Y_{Fe} is the far-field steel surface level of 106mm, and Y_D is the domain height of 150mm. Heat flux across the boundary is set to zero. To avoid convergence issues, any fluid that would reenter the domain was given a "backflow" temperature of T_b that varied linearly from x=0mm (mold hot face) to x=1.3 for slag and from x=10mm to x=25mm for steel. (Values are given in Table 3.1)

3.3.4 Zero-gradient walls

The rest of the fluid domain boundary at y=0 or x=100mm (except for the steel inlet and slag & steel outlet) is a zero gradient wall, where normal velocities, tangential velocity gradients and normal heat flux are all set to zero.

At x=100, y>92 or y<65

$$v_x = 0;\ \frac{\partial v_y}{\partial x} = 0;\ K_{eff}\frac{\partial T}{\partial x} = 0 \qquad (3.25)$$

At y=0, x>25

$$v_y = 0;\ \frac{\partial v_x}{\partial y} = 0;\ K_{eff}\frac{\partial T}{\partial y} = 0 \qquad (3.26)$$

3.3.5 Mold cold face

The mold surface that approximates the circular cooling channels in Zhang's experiment[3] is a convection boundary that removes heat to the cooling water:

$$q_c = h_c(T_w - T) \qquad (3.27)$$

where q_c is the cold-face heat flux, h_c is the effective convection heat-transfer coefficient, and T_w is the average water temperature.

The effective convection heat-transfer coefficient, h_c, and effective mold thickness d are calculated through a reduced order (ROM) heat transfer model explained in section 3.4.

3.3.6 Mold top and bottom wall

The top and bottom surface of the mold are insulated surfaces because heat transfer from those surfaces is negligible[49] and heat flow is mainly perpendicular to the mold hot face.

$$K_{Cu}\frac{\partial T}{\partial y}=0 \qquad (3.28)$$

3.3.7 Mold domain velocity

The entire solid (mold) portion of the domain is prescribed a velocity according to the mold oscillation:

$$v_x=0;\ \ v_y=v_m=\pi sf\,\sin\{2\pi f(t-t_0)\} \qquad (3.29)$$

Where s=stroke, f=frequency, t is time and t_0 is the time when the mold is at its lowest position, and just about to gain positive (upward) y velocity.

3.3.8 Mold Hotface Interface (coupled wall[48])

The interface between the fluid and mold domain is coupled in both velocity and heat flux. This interface moves with the mold velocity ($v_x=0;\ v_y=v_m$) and has this form of no-slip condition on the fluid side. The instantaneous heat flux between points on the mold and the fluid domain that are currently adjacent are made the same at every time. Details of this method are available elsewhere.[48]

3.3.9 Slag & Steel Interface

The internal boundary representing the slag and steel interface is interpreted from the VOF model results, where$0\le\alpha_{Fe}\le 1$. The part of this slag &steel interface away from meniscus (x>5mm) is set to have a temperature equal to or higher than T_{liq}. This provides additional heat to the domain to stabilize its temperature and prevent solidification at the slag & steel interface.

3.3.10 Solid steel shell

A pseudo fixed-velocity boundary condition is applied to the solid state steel defined via the following condition:

$$\begin{cases} T \leq T_{sol} \\ \alpha_{Fe} \geq 0.9 \end{cases} \quad (3.30)$$

Where this condition is met, velocity is fixed to casting speed ($v_x = 0;\ v_y = v_c$) during the finite volume method numerical implementation using ANSYS Fluent[48], details of this method will be discussed in section 3.6.

3.4 Reduced Order Model for Mold Heat Transfer

A reduced order heat transfer model is employed to simply the 3D geometry of a real mold geometry into a 2D rectangle with the same heat transfer behavior. The geometry of the mold used in Zhang's experiment[3] is shown in Figure 3.3 (all dimensions in mm). The mold wall was wrapped by an extractor on 3 faces; the other face was in contact with steel. Two water holes are drilled through the mold wall vertically, and pairs of thermocouples are placed at several heights in the mold wall. The goal of the reduced order model (ROM) is to create 2D rectangular mold in the xy plane that has the same effective heat transfer characteristics so that it can be used in the main transient coupled thermo-flow model.

A simple scaling shows that heat transfer in the mold wall in the vertical y direction is much smaller than in the horizontal x direction, so the heat transfer in a xz plane slice can be modeled independently. The ROM simplifies the real 3D to a 2D problem, eliminating the z-direction because the 2D slice in the xz plane is transformed into a 1D heat transfer model in the x direction, according to the equations given in the next section.

3.4.1 Two dimensional model in xz plane

A 2D steady state heat transfer calculation is performed in the xz plane. The domain of this "transverse" model includes half of the mold with a symmetry plane, as shown in Figure 3.4. Both the extractor surface and the symmetry plane are insulated. The mold hot surface has a uniform incoming heat flux of Q. The water channel surface has a convection boundary condition with convection heat-transfer coefficient, h_w, and far field water temperature of $T_w = 10$℃.

The convection heat-transfer coefficient h_w for the circular water channel is calculated to be 9200 W/m^{2}K based on the cooling water velocity (1.5m/s[3]) and the water channel dimensions using an empirical correlation[50]:

$$\begin{cases} Nu = 0.023\xi_L Re^{0.8} Pr^{0.4} \\ \xi_L = 1 + \left(\frac{D}{L}\right)^{0.7} \end{cases} \quad (3.31)$$

This model uses thermal conductivity of 350 W/mK, typical for copper.

The resulting temperature field in Figure 3.4 shows a relatively linear temperature variation below the circular water channel. This indicates that a reduced order 1 dimensional model can be a good approximation to the 2D transverse slice in the xz plane.

Seven cases with different input heat flux Q were run, and sample results from the 2D model are included in Table 3.2. Results with Q=1.1 *MW/m2* were used as the calibration case to set up the 1D model and the rest are used for validation, as explained in the next section.

3.4.2 One dimensional model in x direction

The 1D model has an effective mold width, d, in the x direction extending from x=-d to x=0. The boundary x=0 represents the mold hot face where the same heat flux Q is applied. The boundary x=-d represents the water channel surface and has a convection heat transfer

boundary condition with an effective heat transfer coefficient and the same far field water temperature, T_w. Temperature at the 1D hot and cold face is set to the 2D hot face average temperature T_h and the lower half water channel to the average T_c respectively as a calibration measure to determine the effective mold wall width d and cold face heat transfer coefficient, h_c.

To determine h_c and d, the following equations, based on energy conservation, are solved:

Hot face boundary condition:

$$K_{Cu}(T_h - T_c)/d = Q \quad (3.32)$$

Cold face boundary condition:

$$Q = h_c(T_w - T_c) \quad (3.33)$$

With the cold face temperature T_c and hot face temperature T_h from the 2D transverse-model calibration case, the effective mold width d is determined to be 12.327mm and the effective heat transfer coefficient h_c is 10,542.9 W/mK.

The hot and cold face temperatures predicted by the 1D model using different heat flux input are then compared to those from the 2D transverse model as validation, as shown in Table 3.2. The validation results show that the 1D model is an accurate representation of the 2D actual mold geometry with different input heat flux. Hence, by extending the 1D model in the y direction, a rectangular 2D mold can be obtained that accurately represents the heat transfer inside the full 3D mold wall.

As a side product of the ROM, effective thermocouple locations are calculated using a similar calibration method as for the effective mold wall thickness.

$$K_{Cu}(T_h - T_{TC})/d_{TC} = Q \quad (3.34)$$

By plugging in the thermocouple temperature from the 2D transverse model, effective thermocouple locations in the ROM model are determined to be at x=-3.048mm and x=-8.095mm.

3.5 Material Properties

Values for the constant material properties are given in Table 3.3, and other material properties are discussed below.

3.5.1 Powder/molten slag properties

Slag enters the fluid domain as powder at the top surface, it sinters and melt with increased temperature, and then re-solidifies against the mold wall. Slag has different temperature dependent properties depend on whether it is in the melting process or re-solidifying process. Material properties for solidifying slag behavior are applied near the mold wall, with the location constraint $x \leq 3mm$, while properties for melting behavior are applied to the rest of the domain. Temperature-dependent values for the viscosity, thermal conductivity and specific heat used in this model are taken from the previous simulation model by Jonayat et al.[34], and can be found in Figure 3.5 through Figure 3.7. Density of the slag is fixed at $2500kg/m^3$.

3.5.2 Steel liquidus and solidus temperature

Liquidus and solidus temperatures are calculated for the chosen steel alloy composition in Table 3.4, using the following equation:[51]

$$T_{liq} = T_{pure} - \sum_i m_i \cdot C_{0,i} \qquad (3.35)$$

$$T_{sol} = T_{pure} - \sum_i m_i \cdot C_{L,i}$$

where T_{pure} is the melting point of pure iron (1536℃), m_i is the slope of the liquidus line of each solute element in the pseudobinary Fe-phase diagram, given in Table 3.5, $C_{0,i}$ is the initial composition of each alloy components and $C_{L,i}$ is the concentration of each solute elements at the interface in the liquid.

By the lever-rule model,

$$C_{L,i} = \frac{C_{0,i}}{1 - (1 - k_i) f_s} \qquad (3.36)$$

Where k_i is the equilibrium partition coefficient for each alloy component and f_s is the solid fraction.

By setting solid fraction, f_s to 1 and using the equilibrium partition coefficient for δ - ferrite, $k^{\delta/L}$, $C_{L,i}$ is calculated and tabulated for each alloy component in Table 3.5.

Finally, liquidus and solidus temperatures are calculated to be 1526.12℃ and 1482.09℃, giving a 44° solidification range. However, in order to allow a better implementation of the shell velocity fixing method (detailed in section 3.6), this model uses a 5℃ solidification range where liquidus temperature is set to 1526.85℃ (1800K). This corresponds to a steel alloy with fewer residual elements.

3.5.3 Steel viscosity

Plasticity dominates solid steel mechanical behavior near the solidus temperature, and stress depends more on strain rate than strain. Hence, during solidification, viscosity is an appropriate property for modeling the mechanical behavior of steel.

The effective steel viscosity near the solidus temperature is estimated using the power law model[52] for δ-ferrite, as the carbon content is lower than 0.5%.

$$\begin{cases} \dot{\bar{\epsilon}}\,(1/s) = 0.1{F_\delta}^n \\ F_\delta = \dfrac{\bar{\sigma}\,(Mpa)}{f_c \cdot \left(\dfrac{T(K)}{300}\right)^{-5.52} \cdot (1+1000\bar{\epsilon})^m} \\ f_c = 13678 \times (pct\ C)^{-0.0556} \\ n = (1.617 \times 10^{-4} \times T(K) - 0.06166)^{-1} \\ m = -9.4156 \times 10^{-5} \times T(K) + 0.349501 \end{cases} \tag{3.37}$$

where $\bar{\epsilon}$, $\dot{\bar{\epsilon}}$, are effective (Von-Mises) inelastic strain and strain rate, and $\bar{\sigma}$ is effective stress.

By assuming zero inelastic strain and considering a pure shear loading condition, viscosity can be calculated based on its definition

$$f_c \cdot \left(\frac{T(K)}{300}\right)^{-5.52} \frac{1}{\dot{\bar{\epsilon}}} (10\dot{\bar{\epsilon}})^{\frac{1}{n}} = \frac{\bar{\sigma}}{\dot{\bar{\epsilon}}} = \frac{\sqrt{3}\tau_{xy}}{\frac{2}{\sqrt{3}}\dot{\epsilon}_{xy}} = \frac{3}{2}\frac{\tau_{xy}}{\dot{\epsilon}_{xy}} = \frac{3}{2}\mu_{st} \tag{3.38}$$

where τ_{xy}, and $\dot{\epsilon}_{xy}$ are the stress and inelastic strain rate in a pure shear condition corresponding to the effective stress and strain rate.

Viscosity at T=1800K under different carbon contents and strain rates are calculated and presented in Table 3.6. As can be seen, steel viscosity upon solidification is around $10^6\ Pa \cdot s$ to $10^7\ Pa \cdot s$. However, in order to avoid convergence issues during finite volume method calculation, the current model uses viscosity up to $10^3\ Pa \cdot s$. The temperature dependent steel viscosity function is shown in Figure 3.8. The rigidness of the steel shell after solidification is achieved by the boundary in section 3.3.10.

3.6 Solution procedure

The coupled transient energy equation and incompressible Navier-Stokes equations are discretized using the finite volume method and solved on a fixed quadrilateral mesh for temperature, pressure, and velocity field using ANSYS FLUENT 13.0.[48]

While velocities and turbulence quantities are saved in cell-centers, pressure is computed in the center of the faces between cells using the PRESTO scheme, which mimics the staggered arrangement[48]. Spatial discretization used second-order upwinding for advection terms and a second-order central-difference scheme with a least-squares gradient method for the diffusion terms. A first-order implicit scheme is used for discretizing time for the transient terms. A pressure-based segregated algorithm, Pressure- Implicit with Splitting of Operators (PISO[48]), is used for coupling pressure and velocity. The VOF equation is solved using explicit time discretization and a geometric reconstruction scheme[48] is applied for face fluxes in cells where the interface is located.

Velocity in cells that constitute the steel shell are altered to match the casting speed at the beginning of each time step, using an "adjust" UDF function in FLUENT[48]. Iterations are then carried out until convergence is reached in each time step, which is defined by the globally scaled[48] continuity residual dropping less than 1.5×10^{-4} and velocity residual dropping less than 4×10^{-4} in both x and y direction. This method is capable of effectively fixing the steel shell velocity as demonstrated in section 4.2. This method is only applied to cells that are located lower in the domain than y= Y_{fix}, where Y_{fix} varies with time during a oscillation cycle to account for the height change of the newly formed shell tip, as shown in Figure 3.2.

The initial condition for the full transient thermal-flow-solidification model is created in several steps. First, the fluid domain is prescribed an estimated phase fraction field with a

uniform slag gap thickness of 1.3mm combined with a slag and steel interface profiles calculated with Bikerman's equation[13],

$$x = x_0 - \sqrt{2b^2 - y^2} + \frac{b}{\sqrt{2}} \ln \frac{b\sqrt{2} + \sqrt{2b^2 - y^2}}{y} \quad (3.39)$$

Where,

$$x_0 = b - \frac{b}{\sqrt{2}} \ln\left(\sqrt{2} + 1\right) \;\; and \;\; b^2 = \frac{2\gamma_{Fe(l)-sl}}{g(\rho_{Fe} - \rho_{sl})} \quad (3.40)$$

where, x= horizontal distance from the wall where the phases meet, y = vertical distance from the free surface.

Then, the guess is improved by solving the steady isothermal flow equations including the VOF model Eqn. (*3.1* - (*3.8*, assuming constant slag viscosity (0.1 Pa·s) and no mold or shell movement.

Next, based on the resulting phase fraction field, the initial temperature field is obtained by solving the steady state energy equation system, Eqn. (*3.12* - (*3.17* 错误!未找到引用源。, with no flow. An initial shell is also prescribed in the model at this step, based on a 5.6mm shell thickness at 100mm down the mold. Temperature of the liquid steel to the right of the shell profile is fixed at the liquidus temperature, and the solid shell thickness profile is prescribed by the following:

$$y(mm) = d_g + 0.56 * \sqrt{100 - x(mm)} \quad (3.41)$$

Where d_g is the initial slag gap thickness, (set to be 1.3mm).

After this obtaining this rough estimate of the temperature field, the initial flow field is calculated inside the fluid domain by solving the fully coupled transient thermal-flow

equation system, Eqn. （*3.1* - （*3.23* without mold oscillation until the result reaches steady state, which takes 4.65s simulation time.

Finally, oscillation is added to the model, and the complete model is run until convergence, defined when the conditions at the end of the cycle match the conditions at the beginning of the cycle. This is typically obtained after 12.5 cycles (periods) of oscillation, which is sufficient time for the entire shell to pass through the domain (domain length divided by the casting speed).

With a fixed time step of 10^{-5} seconds and a fine mesh (141,241 cells with the smallest cells being $0.05\times 0.05\ mm$ near the phase interface and mold hot face), it takes about 1 day to complete one oscillation cycle of the simulation on an Intel Xeon CPU with 6×2.6GHz cores desktop Windows computer.

Further details of the set up procedure in FLUENT are described in the Appendix.

3.7 Figures

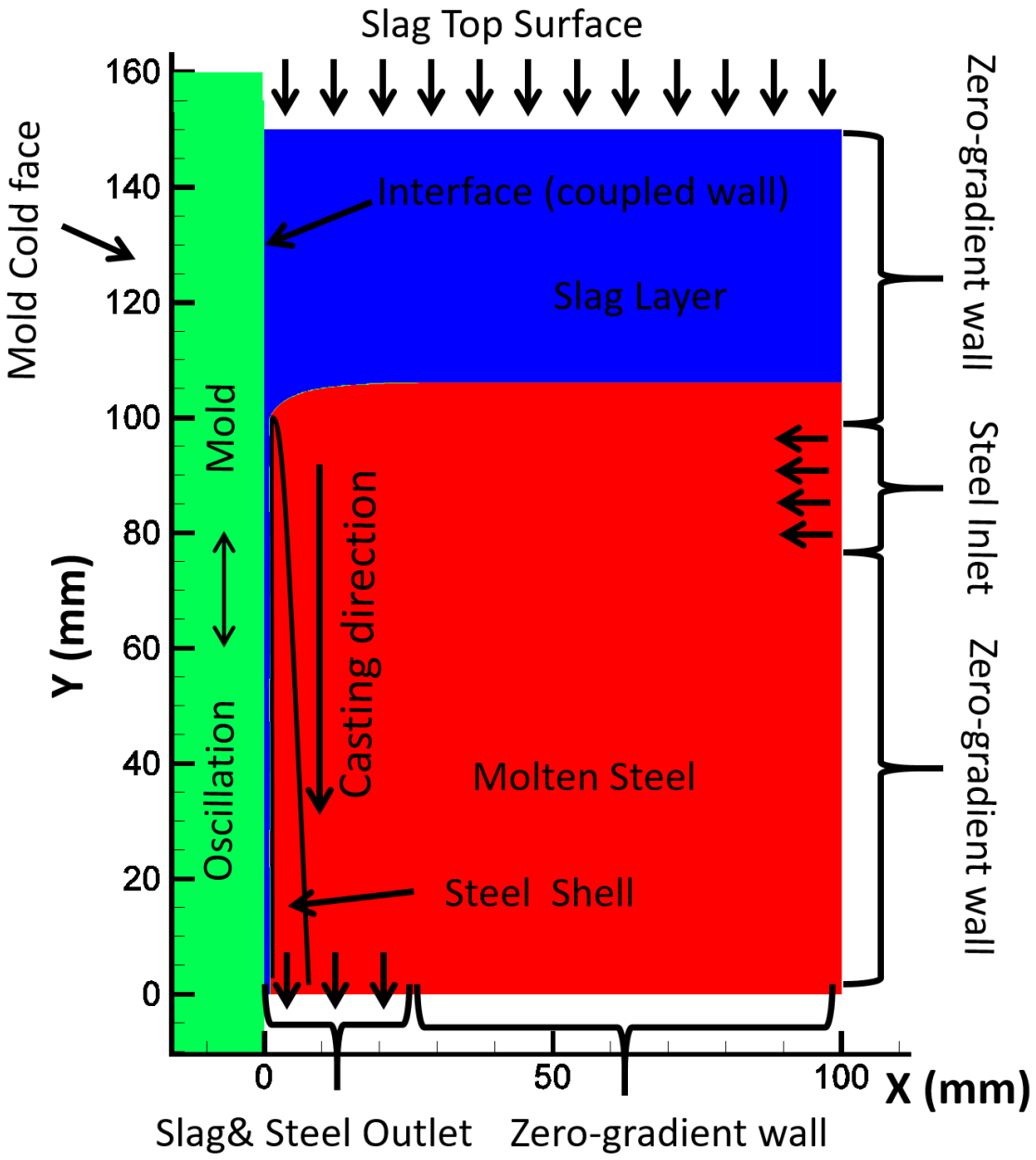

Figure 3.1: Schematic of main model domain and boundaries

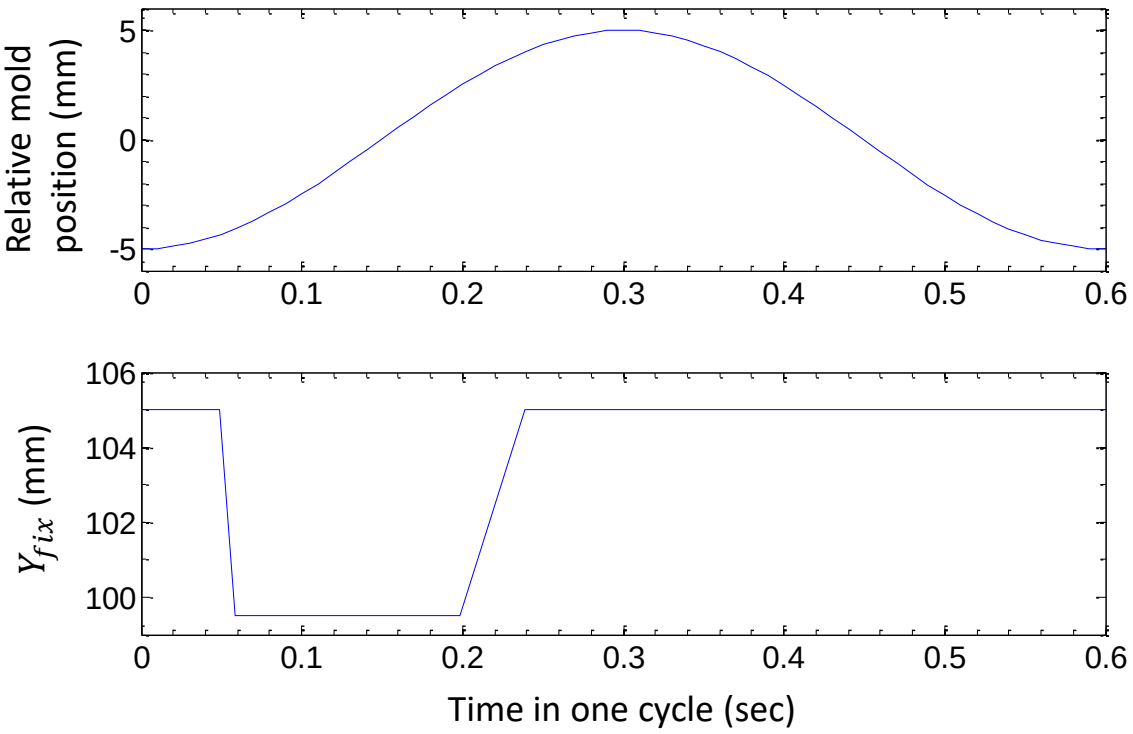

Figure 3.2: Vertical location threshold for the velocity fix boundary condition

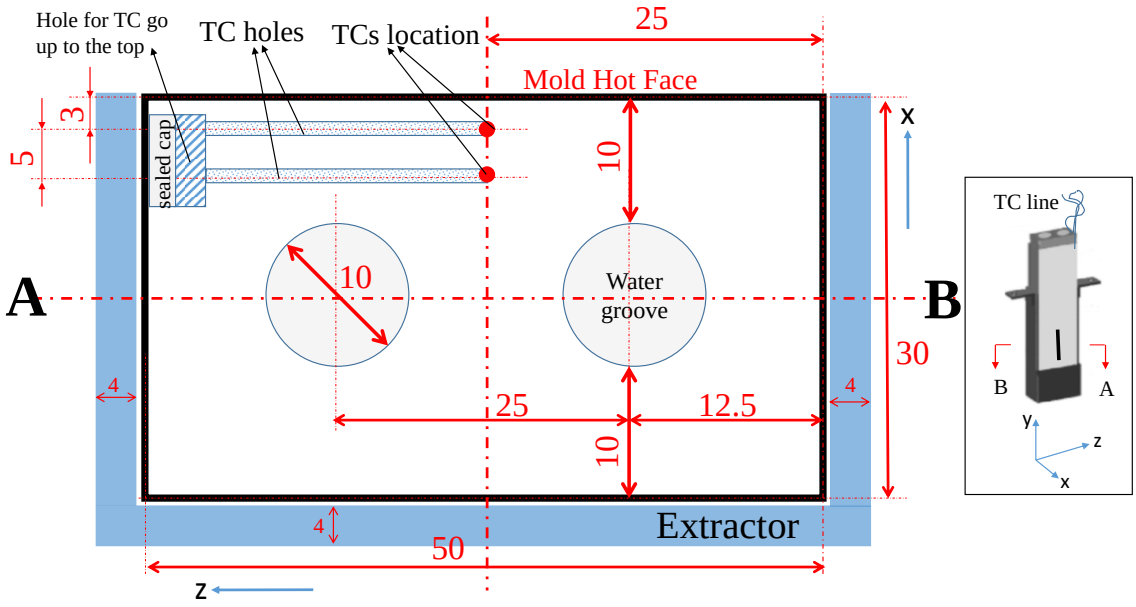

Figure 3.3: Mold cross-section geometry in Zhang's experiment

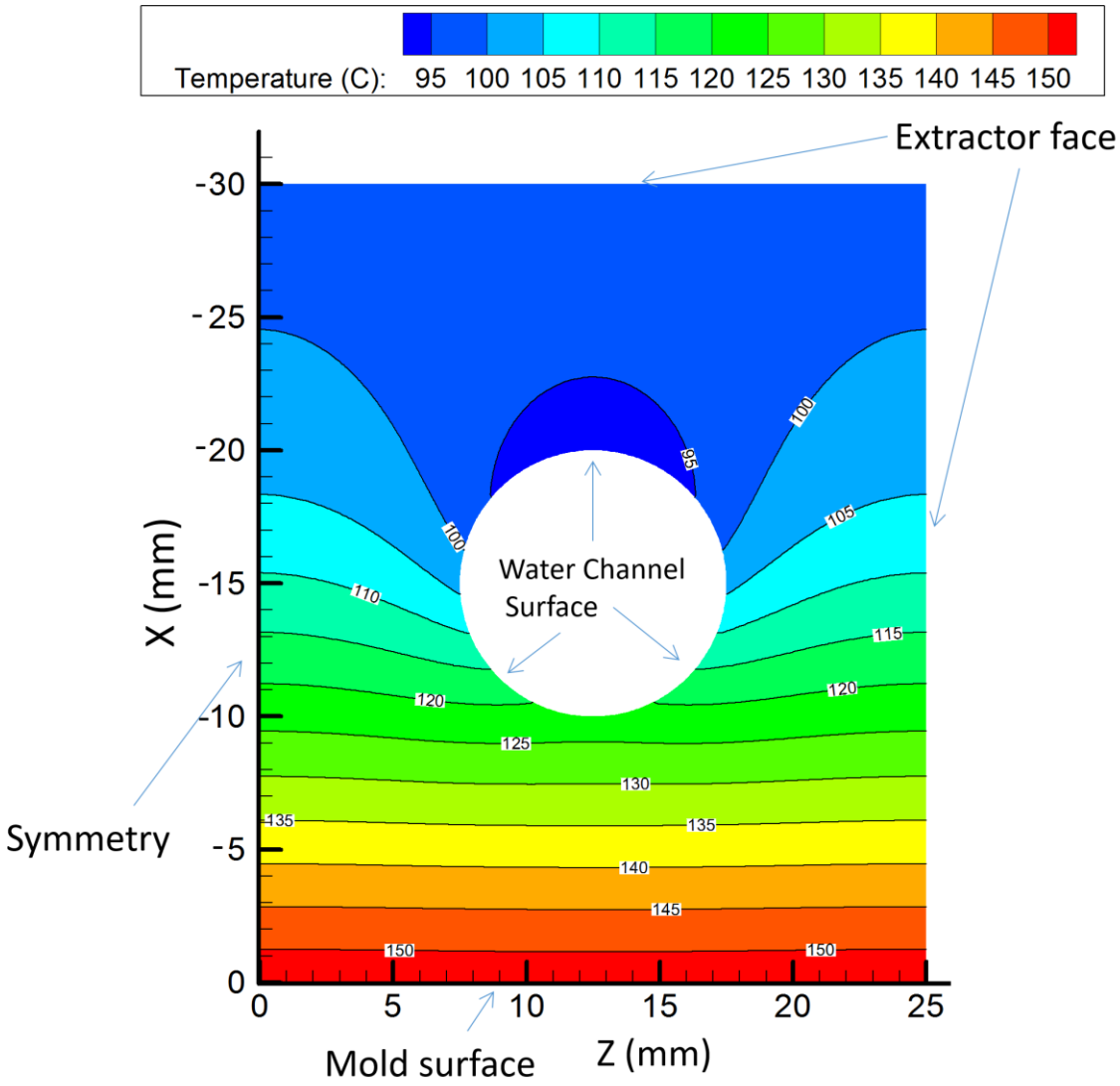

Figure 3.4: Domain and predicted temperature for the 2D mold simulation

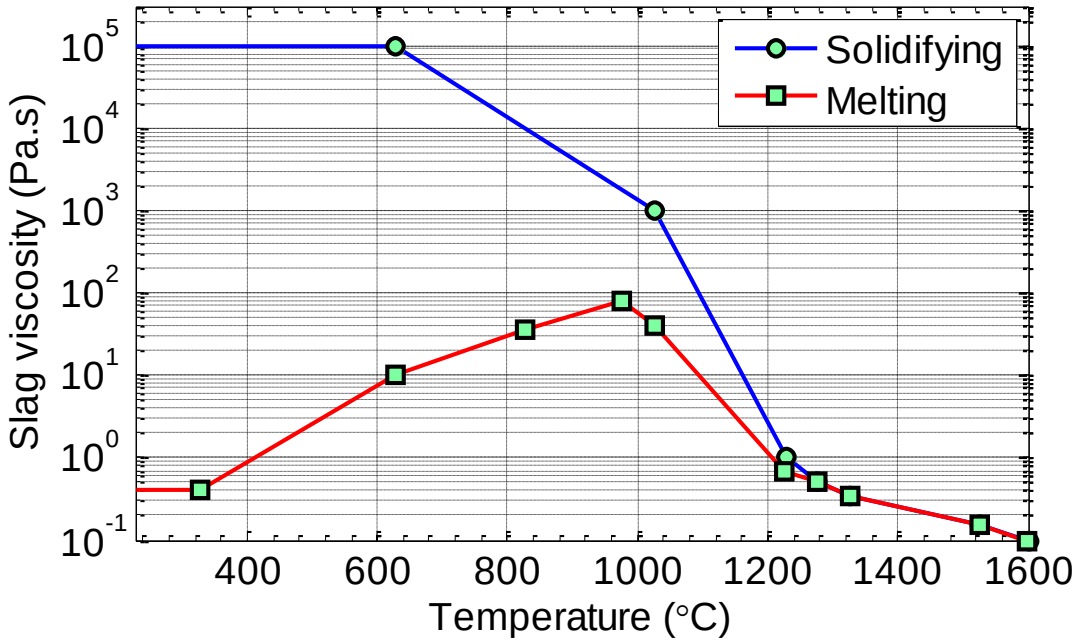

Figure 3.5: Temperature dependent slag viscosity model during solidification and melting

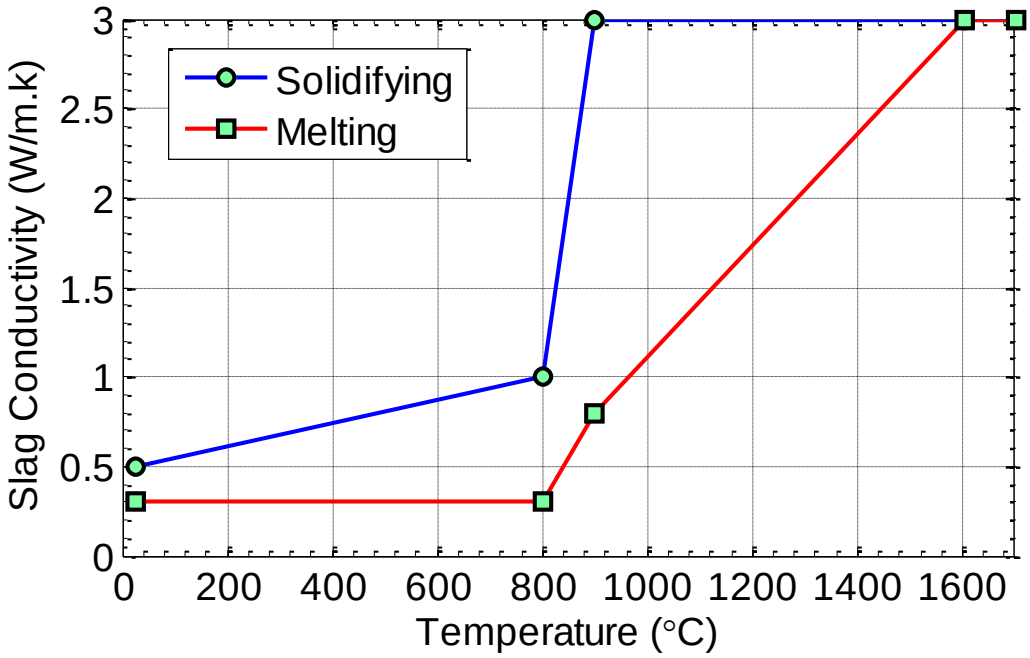

Figure 3.6: Temperature dependent slag thermal conductivity model during solidification and melting

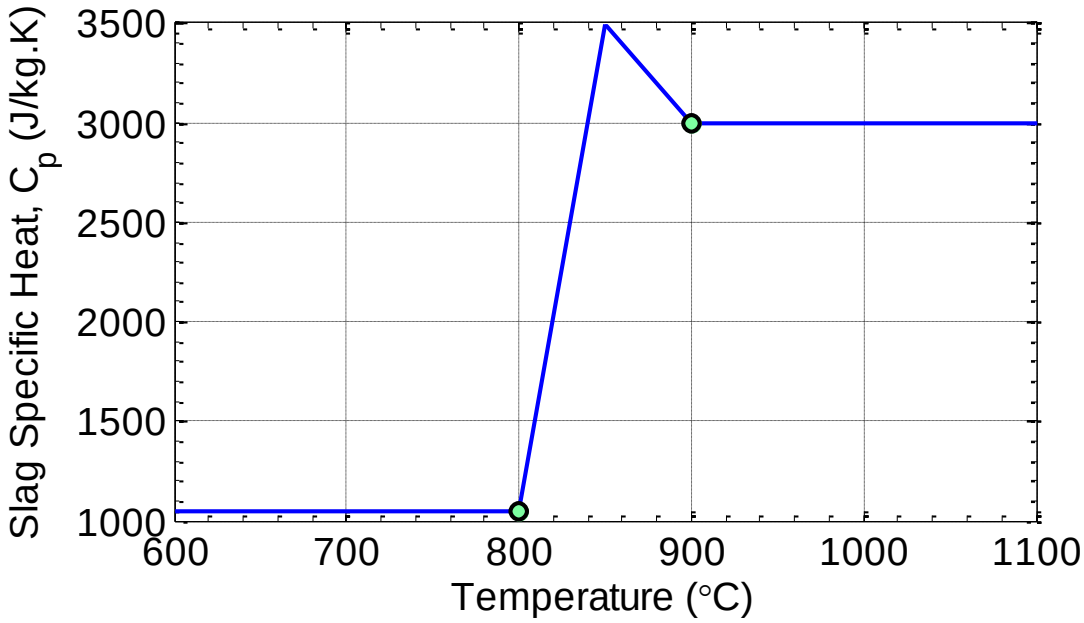

Figure 3.7: Temperature dependent slag specific heat

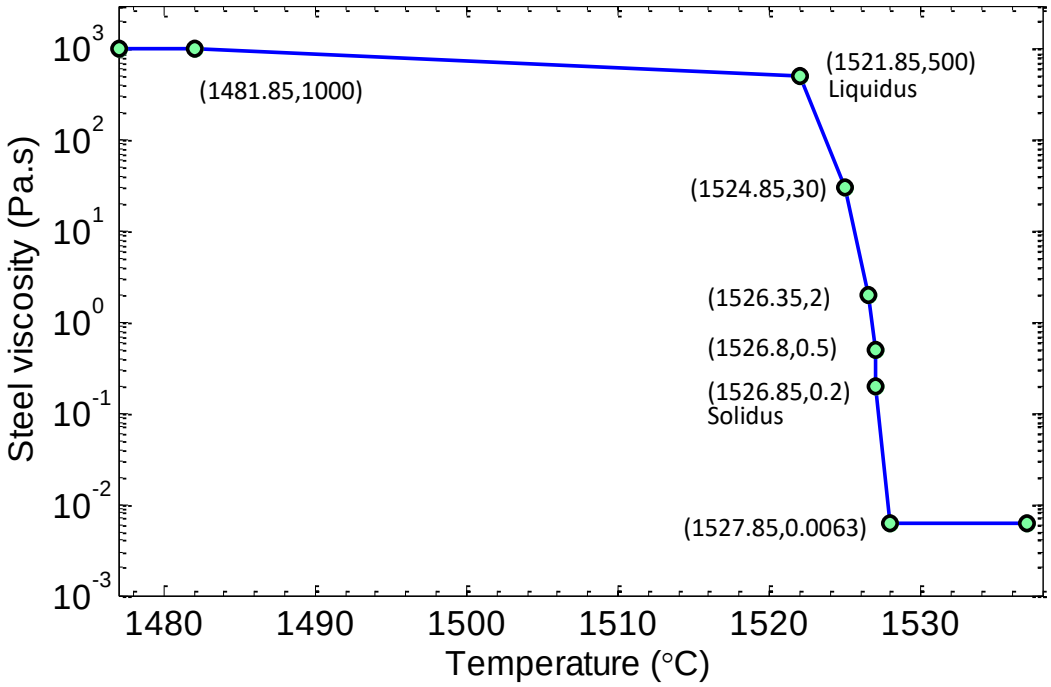

Figure 3.8: Temperature dependent steel viscosity

3.8 Tables

Table 3.1 Variables used in model

Boundary Conditions		***Casting Conditions***	
$\boldsymbol{p_i}$	*1 atm*	v_c	*0.01 m/s (0.6m/min)*
$\boldsymbol{p_o}$	*1 atm+8358Pa*	*s*	*10.0mm*
$\boldsymbol{T_a}$	*300*℃	*f*	*1.67Hz*
$\boldsymbol{T_b}$	*207*℃*-1257*℃ *(slag)*		
	1532℃*-1537*℃ *(steel)*	***Casting Conditions***	
$\boldsymbol{h_c}$	*10,542.9* W/m^2K	*d*	*12.327mm*
$\boldsymbol{T_i}$	*1,536.85* ℃	*D*	*10mm*
$\boldsymbol{T_w}$	*10*℃	*L*	*330mm*

Table 3.2: ROM mold heat transfer results with different heat flux input

	Heat Flux Q (W/m^2)	T_c *2D*	T_h *2D*	T_c *1D*	T_h *1D*
Calibration	1.1×10^6	387.49	423.17	387.49	423.17
Validation	2.0×10^6	472.85	537.73	472.85	537.73
	5.0×10^5	330.58	346.80	330.58	346.80
	2.0×10^5	302.12	308.61	302.12	308.61
	1.0×10^5	292.64	295.88	292.64	295.88
	3.0×10^4	286.00	286.97	286.00	286.97
	1.0×10^4	284.10	284.42	284.10	284.42

Table 3.3: Material property for steel and copper (mold)

Property/Material	*Steel*	*Cu (Mold)*	*Unit*
Density, ρ	*7000*	*8900*	kg/m^3
Specific heat, C_p	*700*	*385*	$J/kg\ K$
Thermal Conductivity, K	*30*	*350*	$W/m\ K$
Latent heat, ΔH_{Fe}	*2.72*$\times 10^5$	---	J/kg

Table 3.4: Alloy composition for the steel grade used in Zhang's experiment

Alloy composition	*C*	*Si*	*Mn*	*P*	*Si*
Weight percentage	0.08	0.03	0.4	0.02	0.02

Table 3.5: Equilibrium partition coefficients, liquidus line slopes of the solute elements[51][53][54][55][56]

	$C_{0,i}$ (pct wt)	$k^{\delta/L}$	$C_{L,i}$ (pct wt)	m_i (°C/pct)	$m_i \times C_{L,i}$ (°C)
C	0.08	0.19	0.42	78	32.8
Si	0.03	0.77	0.039	7.6	0.3
Mn	0.4	0.76	0.53	4.9	2.6
P	0.02	0.23	0.087	34.4	3.0
Si	0.02	0.05	0.40	38	15.2

Table 3.6: Viscosity of steel calculated with power law for different carbon contents and strain rates

Carbon content (%)	*0.1*	*0.01*	*0.001*	*0.001*	*0.001*
Von-Mises Strain Rate ($\frac{1}{s}$)	*0.01*	*0.01*	*0.01*	*0.1*	1
Viscosity ($Pa \cdot s$)	3.1×10^7	3.5×10^7	4×10^7	6.8×10^6	1.2×10^6

CHAPTER 4: RESULTS

This section presents model results of the fluid flow field, slag gap and steel shell thickness profile, slag consumption and temperatures in the meniscus region. Figure 4.1 shows a typical snapshot of the temperature contours in the entire domain. Thick black lines denote the shell strand boundary while the thick red line means steel/slag phase boundary. Flow velocity is represented by the arrow length and direction. The incoming molten-steel stream induces 2 eddies in the domain and carries 10 degree of superheat towards the meniscus.

4.1 Meniscus flow field results

The velocity and temperature field variations for one oscillation cycle are shown in Figure 4.2 (a) - (h); the red line represents the slag and molten steel interface ($\alpha_{Fe} = 0.5$), and the thick black line represents the shell surface ($\beta = 0.5$). Starting from (a), the mold is in its lowest position with zero velocity. The slag rim has been pushed down closest to the meniscus, causing a low steel level in meniscus region, so steel far away from the meniscus starts to fill in. The mold moves upward (during the upstroke) in Figure 4.2 (b) - (d), with maximum upward velocity reached at (c). During this time, the slag rim pulls on the meniscus, sucks slag out of the slag gap, and causes molten steel to overflow the existing partially solidified shell tip, where it solidifies against the mold to form the new shell. A depression forms at the location of overflow, which corresponds to an oscillation mark that is carried down with the moving shell (strand) at the casting speed. The mold reaches its highest position with zero velocity in Figure 4.2 (e) and starts to move downward (beginning the downstroke) after that. The downward moving slag rim squeezes slag into the gap and pushes the interfacial meniscus downward as shown in Figure 4.2 (g)-(h). Steel melt is held inside the shell, hence the shell only grows in thickness but not in length.

This sequence of flow variation and intermittent shell formation by overflow is repeated for every oscillation cycle, producing periodic oscillation marks. The periodic bulging and flattening of the liquid meniscus during PST and NST agrees with previous simulations[31][34] and were observed in lab experiments using mercury or water with silicon oil[36][37]. This intermittent shell forming mechanism appears to agree with Steinruck and Rudischer's simulation[31].

Figure 4.3 (a) - (d) shows a close up view of steel overflow of the meniscus at the shell tip. In Figure 4.3 (b), liquid steel flows over the existing shell. A thin layer of slag is trapped between the liquid steel and shell. The overflowed steel quickly solidifies and forms the new shell in Figure 4.3 (c). The oscillation mark is formed at the junction of the existing shell and the new shell. And inside the OM root is the slag that was entrained in Figure 4.3 (b).

Hook formation is observed when running this model using casting conditions for an industrial caster.[4] (casting speed 25mm/s, oscillation frequency 2.9HZ, Stroke 5.89mm). Figure 4.4 shows a comparison between the hook and OM shapes predicted with this model and an actual etched sample of the surface of the finally solidified strand at the oscillation mark[57]. The model results on the left include a snapshot of the liquid fraction (β) contour during this simulation. Red means $\beta = 1$, and blue means $\beta = 0$; the mold wall is also shown at the left as blue. At the instant of this snapshot, the liquid steel has just overflowed the partly-solidified meniscus, which later is manifested as a hook. The bottom of the overflowed region forms the top of the oscillation mark. Selected velocity vectors are also shown to indicate the flow direction (note that only one in twenty computational cells contains a vector, as the actual mesh is 20 times finer in the thickness direction, with cell size of 0.05mm thick and 1mm long).

4.2 Shell strand surface profile

Figure 4.5 compares the strand surface profile ($\alpha_{Fe} = 0.5\ and\ \beta = 0.5$) at 3 different times, showing the depth and shape of the oscillation marks. The three profiles are plotted in the strand frame of reference, where $Y_s = 0$ is the location of the mean (far-field) surface level (liquid steel – slag interface) at 9.79s. The 3 profiles from the Eulerian model were translated according to the casting speed in order to have the same Y_s value at the same position along the shell surface at the 3 times. The three profiles compare reasonably well, which shows that oscillation mark shape does not evolve much after they form. Each peak on the profile represents the root of an oscillation mark (as the gap containing the slag is at the bottom of the figure). The average pitch is calculated to be 5.72mm with a standard deviation of 1.09mm, which matches reasonably well with the measured pitch[3] of 5.80mm, and with the theoretical pitch ($\boldsymbol{v}_c/f$) of 5.99mm. This variation is typical of measurements of oscillation marks in the mold simulator [3][14] and in the commercial process[10].

The slag gap thickness varies from 1.4mm to 2mm, and averages around 1.6mm, which agrees with the measurement using same casting conditions[3].

Oscillation mark depth (peak to valley) ranges from 0.32mm to 0.55mm with an average value of 0.41mm. This OM depth predicted is typical of measurements in the commercial process [4][16][43] and compares reasonably well with measurements in the simulator using same casting condition[3].

In addition to the overall shape variations, minor "secondary" oscillation marks can be observed in between pairs of normal oscillation marks, at around $Y_s = 10, 16, 20.5, 34, 59$. This is also in agreement with Zhang's experiment[3]. It suggests that these secondary

oscillation marks can be caused by the thermal-fluid flow variations simulated with the current model.

Predicted oscillation mark locations mostly corresponds to the lowest mold position, this is in line with the observation in Figure 4.2 that oscillation mark is formed by overflow at the beginning of PST. The prediction of overflow timing agrees with Badri's[14]and Lopez's findings[38] based on measurements and computational simulation[40] respectively that the root of the OM corresponds to the beginning of PST.

4.3 Shell thickness and solidification factor

Figure 4.6 shows the predicted shell thickness profile ($\beta = 0.5$) against the vertical distance (100-y) down the mold, where y is the vertical coordinate used in the simulation domain. The shell solidification factor K_{sol} is calculated by taking an average slag gap of 1.6mm and fitting the x-coordinate of the shell profile (which is the sum of the solid shell thickness, S, and the slag gap) to the square root law function

$$S(mm) = x - 1.6 = K_{sol}\sqrt{t} \qquad (4.1)$$

Where the solidification time, t, can be expressed as $t(s) = \frac{100-y(mm)}{v_c}$

As shown in the Figure 4.6, the solidification factor K_{sol} is determined to be $1.69 mm/s^{1/2}$, which is very close to Zhang's measurement where the average solidification factor was found to be $1.79 mm/s^{1/2}$. Shell thickness at 100-y=50mm is predicted to be 3.7mm, whereas Zhang measures around 4mm.

Shell thickness simulated near the shell tip is significantly larger than that predicted by the square root law. This is due the two dimensional cooling effect in the meniscus region where the mold (x direction) and the top slag layer (y direction) both extract heat from the

shell tip. The thicker shell tip is observed very often in breakout shells extracted from the commercial process.

Furthermore, two occurrences of slag entrainment beneath the surface of the strand can be observed at 13mm and 28mm down the mold wall. Finally, the shell thickness profile shows variations that correspond with the oscillation marks on the surface. The shell is actually thicker directly beneath each of the first few oscillation marks at the meniscus, owing to the overflow mechanism that formed them. Further down the shell, the shell is slightly thinner beneath the deeper oscillation marks, owing to the local drop in heat transfer rate across the gap. This effect is smaller, however, than the effect of general long-range surface waviness. Regions where the average thickness of the slag gap is thicker for several cm down the mold wall, such as 30-50mm down the mold, have lower heat transfer and a slightly thinner shell than the average profile predicted with Eq. 4.1.

4.4 Slag consumption

Figure 4.7 shows the variation in slag consumption simulated over 5 oscillation cycles. The negative sign means that slag is flowing downward in the casting direction, which corresponds with positive slag consumption. Instantaneous consumption varies in a sinusoidal manner and follows the mold oscillation cycle, which shows how slag consumption is mainly controlled by the oscillating slag rim. This agrees with previous models[34]. This is also illustrated in section 4.1 where the rim pushes slag into the gap during the down-stroke, but draws it upwards out of the gap during the upstroke.

The net consumption of slag is found by integrating the velocity distribution in time over the oscillation cycle. Consumptions for 5 cycles are shown in Table 4.1. Variations between cycles are significant (up to 39% from average) and might be due to variations in pressure

from the slag rim between oscillation cycles, or perhaps due to slag gap thickness variations at the slag outlet. The net average consumption over 5 cycles is predicted to be 9.5g/ms, which is larger than available plant measurements[4], but the difference can be attributed to different slag gap thickness. (1.6mm in this model, compared with 0.67mm to 0.98mm in Shin's measurements[4].)

4.5 Temperature and heat flux

Predicted transient temperature history for the 7 thermocouples closest to the mold hotface ("hot" thermocouples) in Zhang's[3] experiments are shown in Figure 4.8. Thermocouples oscillate with the mold in a moving ("Lagrangian") frame of reference, and the location for all thermocouples (including both the "hot" thermocouples, and the "cold", thermocouples, located in the column that is farther from the hotface) with the neutral vertical mold position is included in Figure 4.10. Predictions for each oscillation cycle are similar, showing that the simulation has reached a pseudo-steady state. Compared to the measured temperatures in Figure 4.10[3], the predictions are about 40K higher. This could be attributed to the fact that temperature measurements still show an upward trend before the mold is pulled out of the melt bath in the experiment, so that possible air bubbles between mold and solid slag and other issues during the initial transient, which are not modelled, may have increased the thermal resistance of the system, lowering mold temperatures.

Figure 4.11 through Figure 4.24 show the transient temperature predicted for each individual thermocouple alongside the instantaneous vertical location of the thermocouple. Thermocouples closer to the mold shows greater cyclic temperature variation. For example, the variation amplitude at around 15.5s is 1.5K (1.5℃, cold) at TC10 and 2.1K (2.1℃, hot) at

TC9. The latter value compares reasonably well with Zhang's measurement at S9[3] of 2.6K (2.6°C). Predictions at the mold surface at the corresponding vertical locations naturally show even higher variations, of 3.2K (3.2°C).

During each oscillation cycle, the predicted temperature increases to a maximum sometime during negative strip time, and then drops. This agrees with previous simulation model[34] and Zhang's measurement[3] near steel level. The general trend of temperature increase during NST can be explain by the fact that during NST, the mold is moving down, so thermocouples above and near to the steel level are getting closer to the meniscus region where the heat flux is very high. The location of the heat flux peak can be seen in the heat flux profiles in Figure 4.25. Note, that distance in this figure is given relative to the far-field meniscus, which has a y-coordinate of 106mm.

A smaller temperature increase is predicted during the PST of each oscillation cycle. This temperature increase is more clear near the steel level, where its maximum amplitude predicted is 0.8K (0.8°C, hot) at TC11. This temperature increase during PST is not reported in the previous simulation model[34] and can be associated with steel overflow that happens during PST. As overflow happens during the PST, the meniscus rises and moves both upwards and towards the mold, which increases the heat flux and the temperature of thermocouples in this vicinity. Thus, when a small increase in temperature is observed in measurements during the PST, this is evidence of meniscus overflow, and likely also of meniscus freezing and hook formation.

4.6 Figures

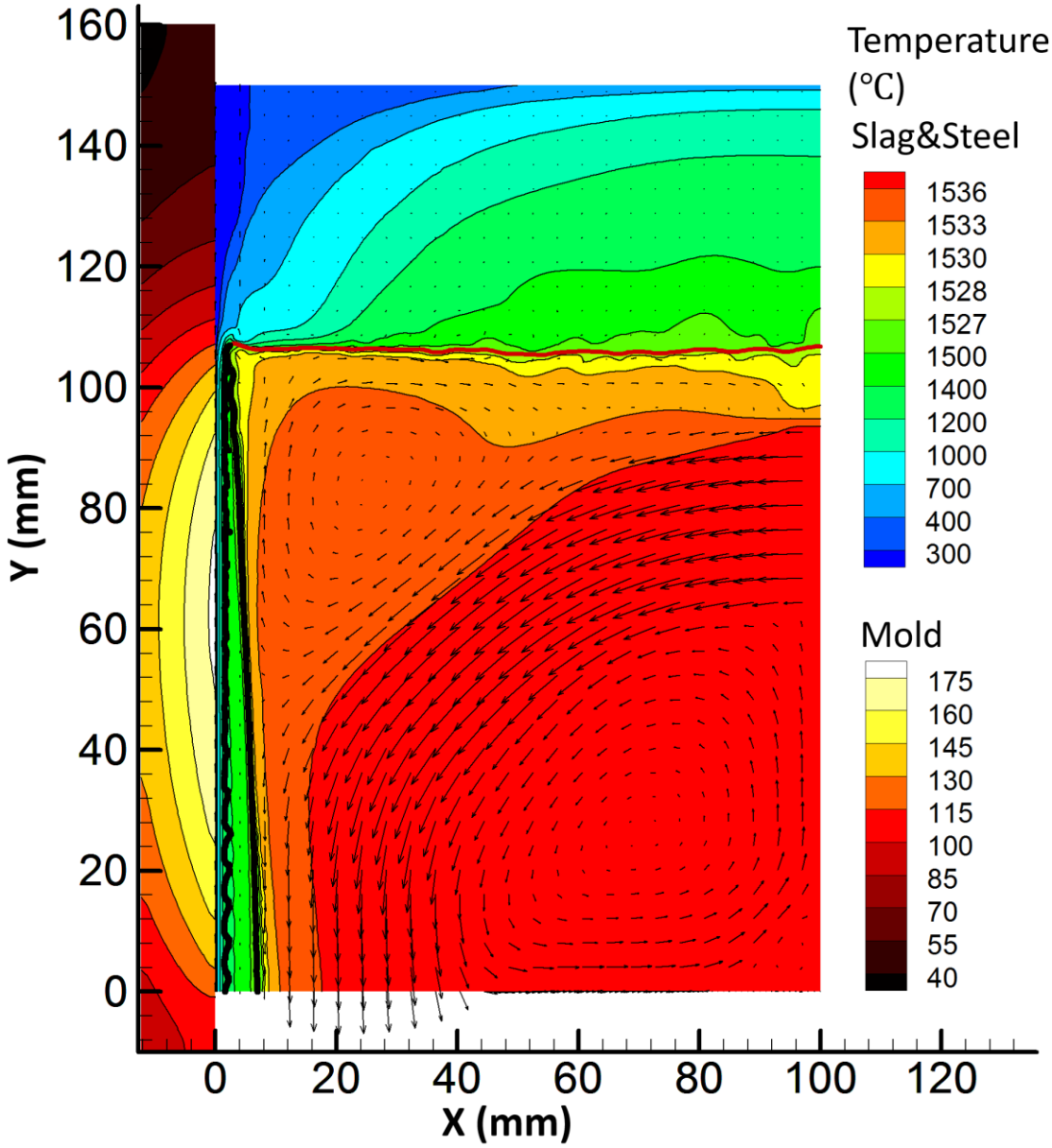

Figure 4.1: Temperature contour of whole domain with flow velocity vetcor

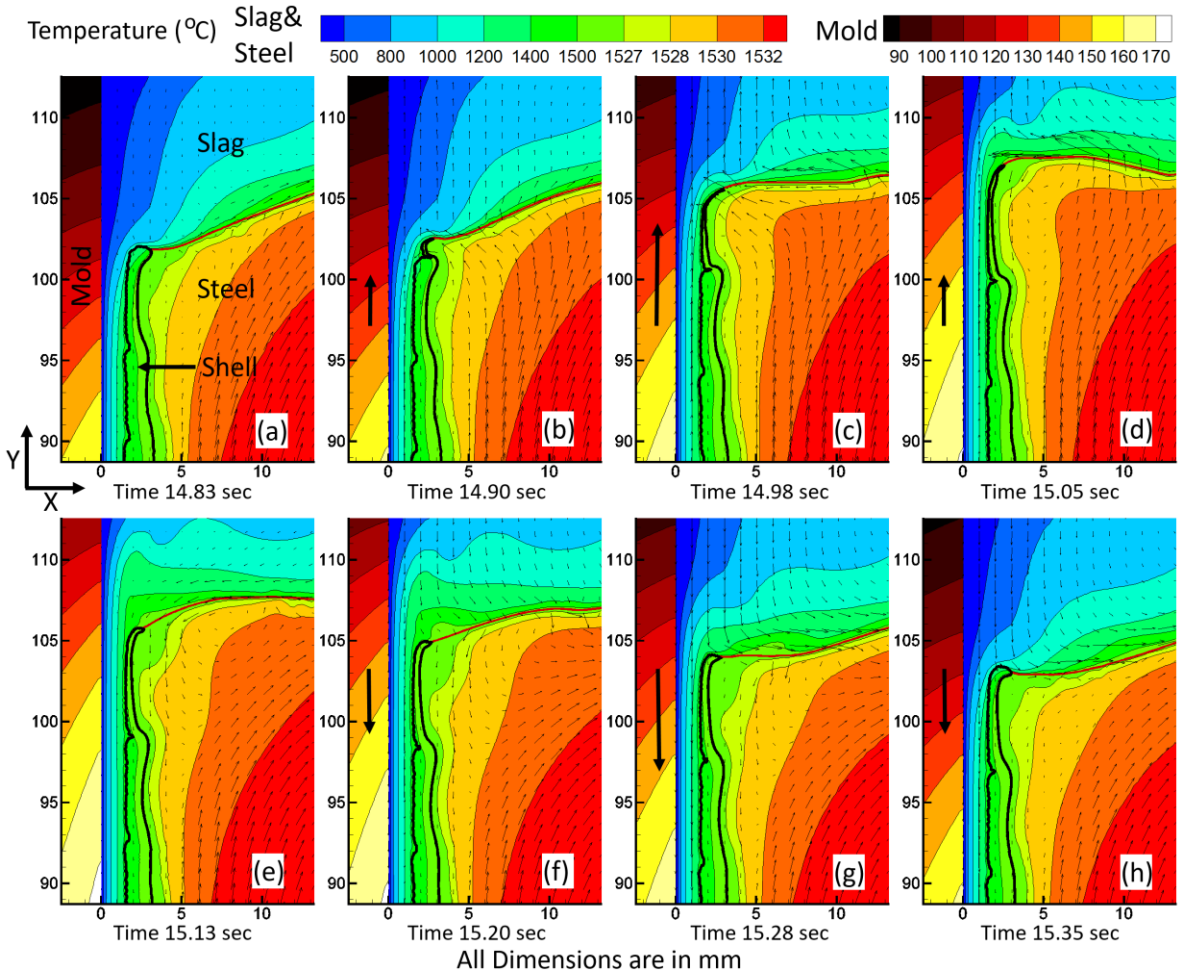

Figure 4.2: Meniscus region events over one oscillation cycle

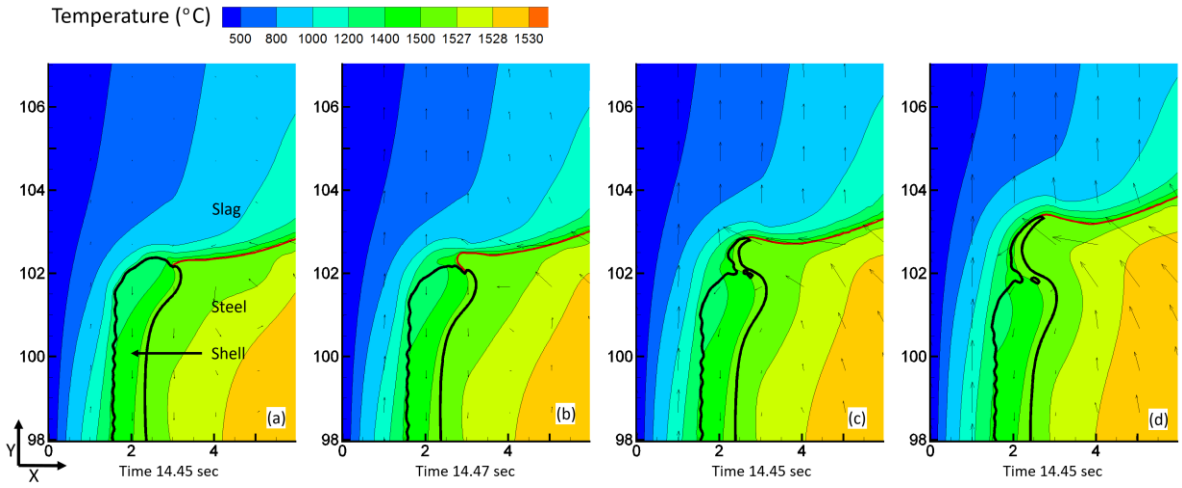

Figure 4.3: Close up view during overflow

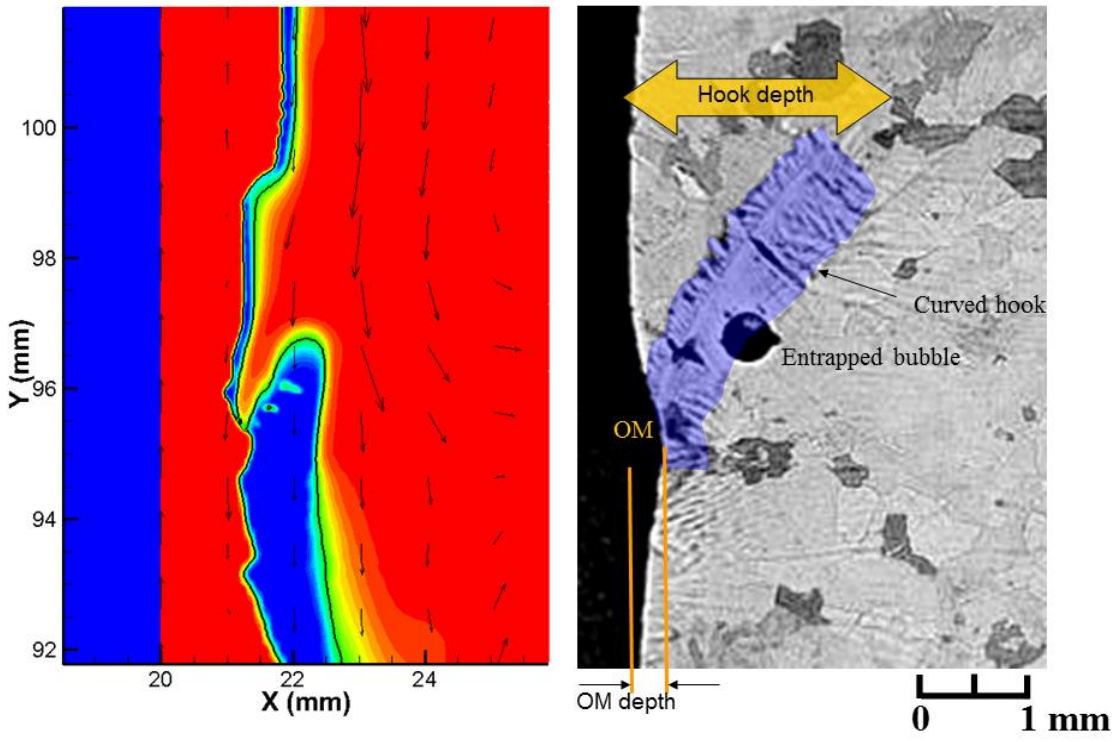

Figure 4.4: Comparison between predicted hook and OM to an etched casting sample[57]

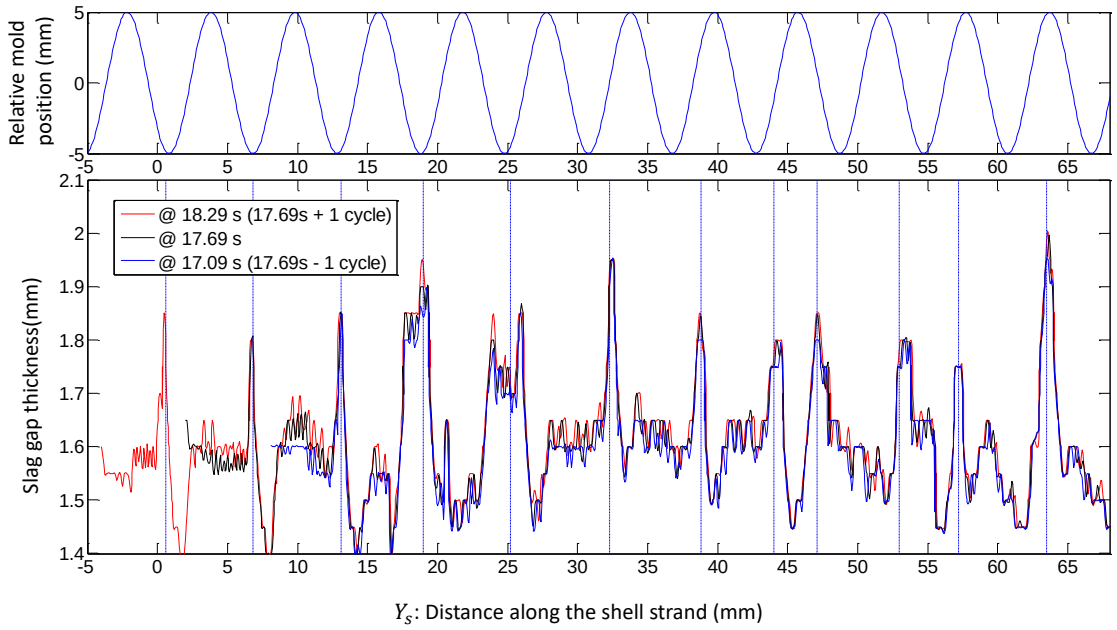

Figure 4.5: Overlay of predicted strand surface profile over 3 cycles

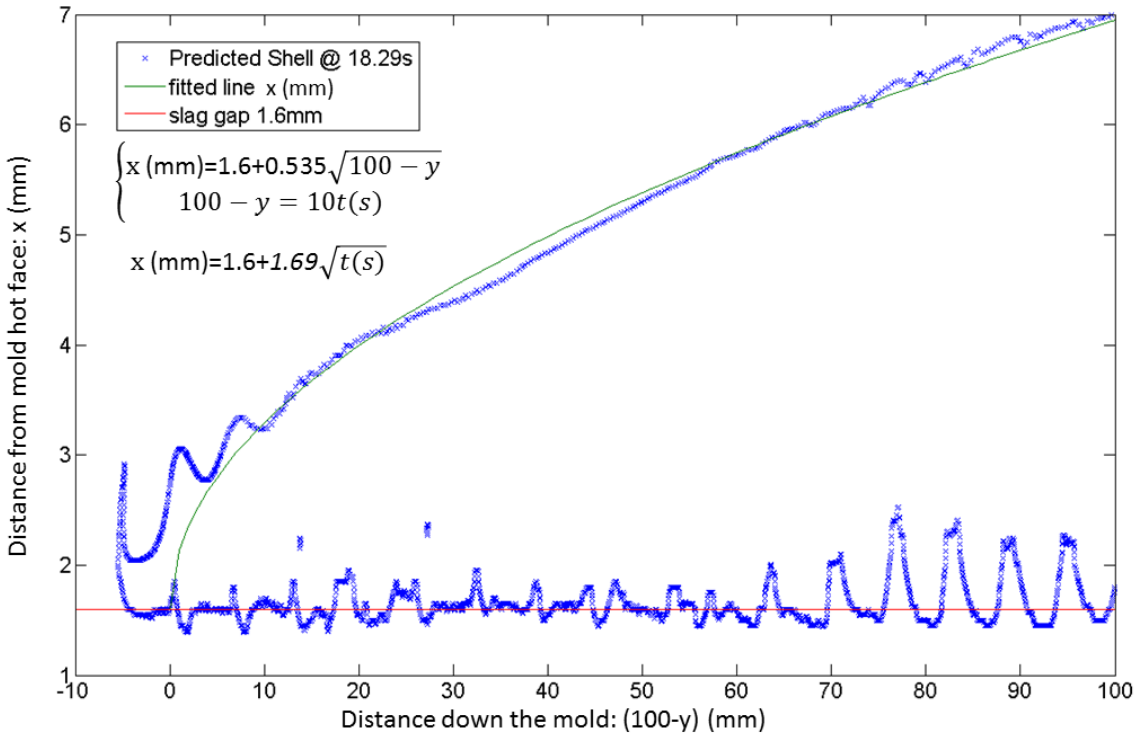

Figure 4.6: Predicted strand profile and solidification factor at 18.29s

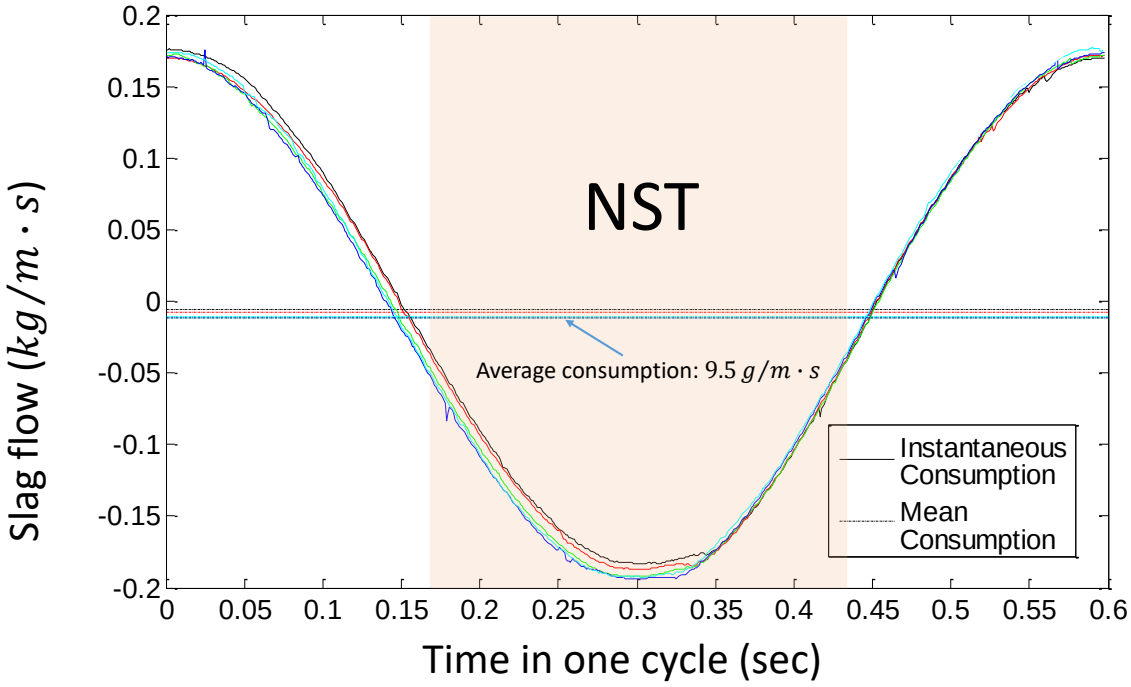

Figure 4.7: Predicted transient slag consumption over 5 cycles

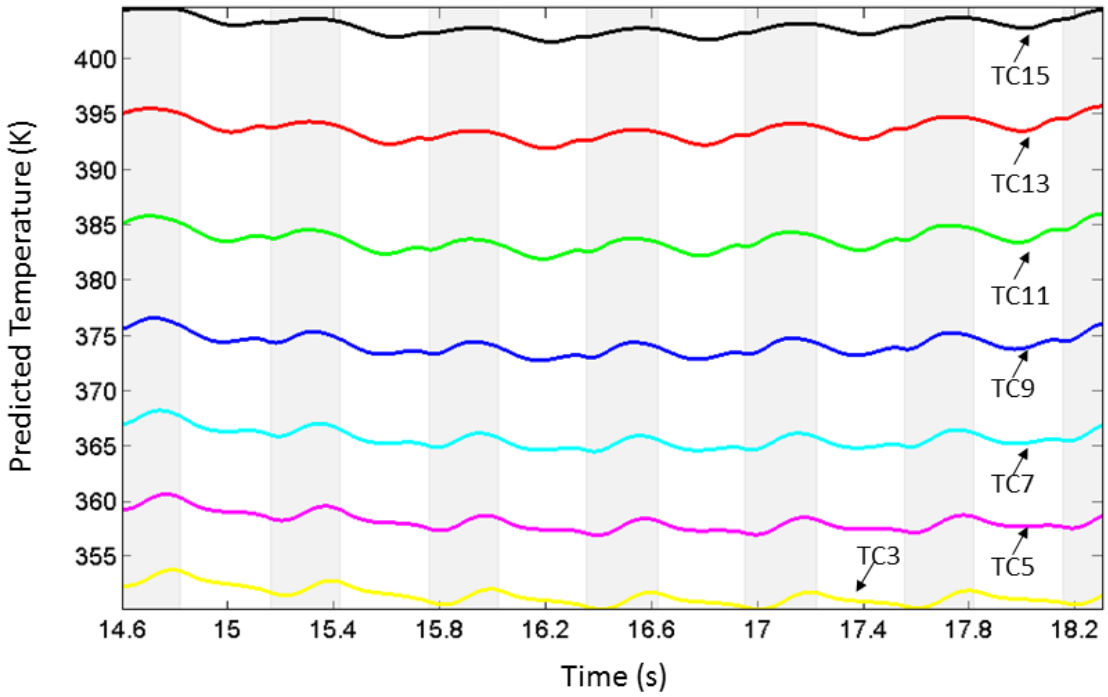

Figure 4.8: Predicted temperatures for the 1st column thermocouples during 6 oscillation cycles. The negative strip time is shaded gray

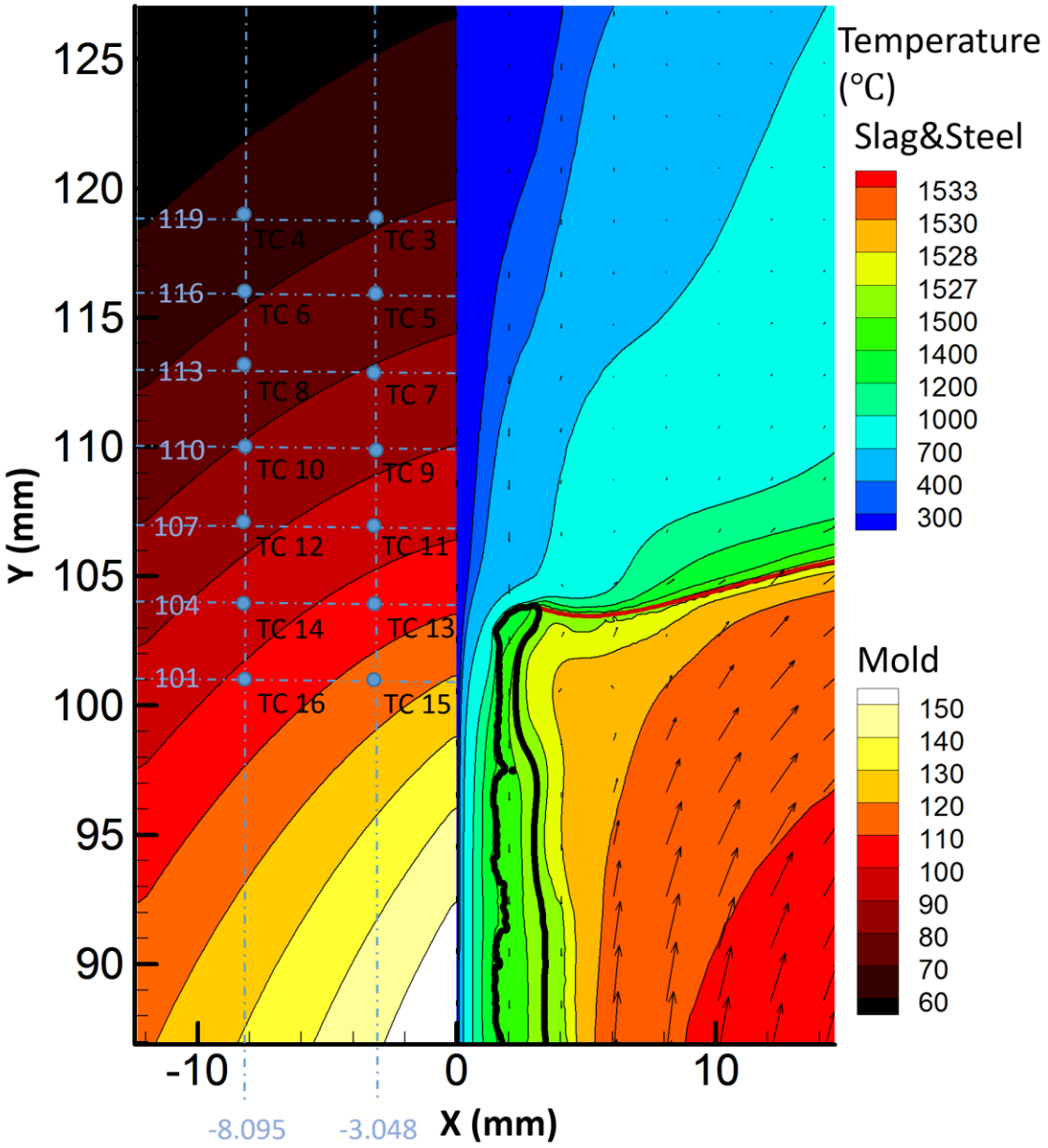

Figure 4.9: Thermocouple location with neutral mold position, simulating Zhang's experiment set up

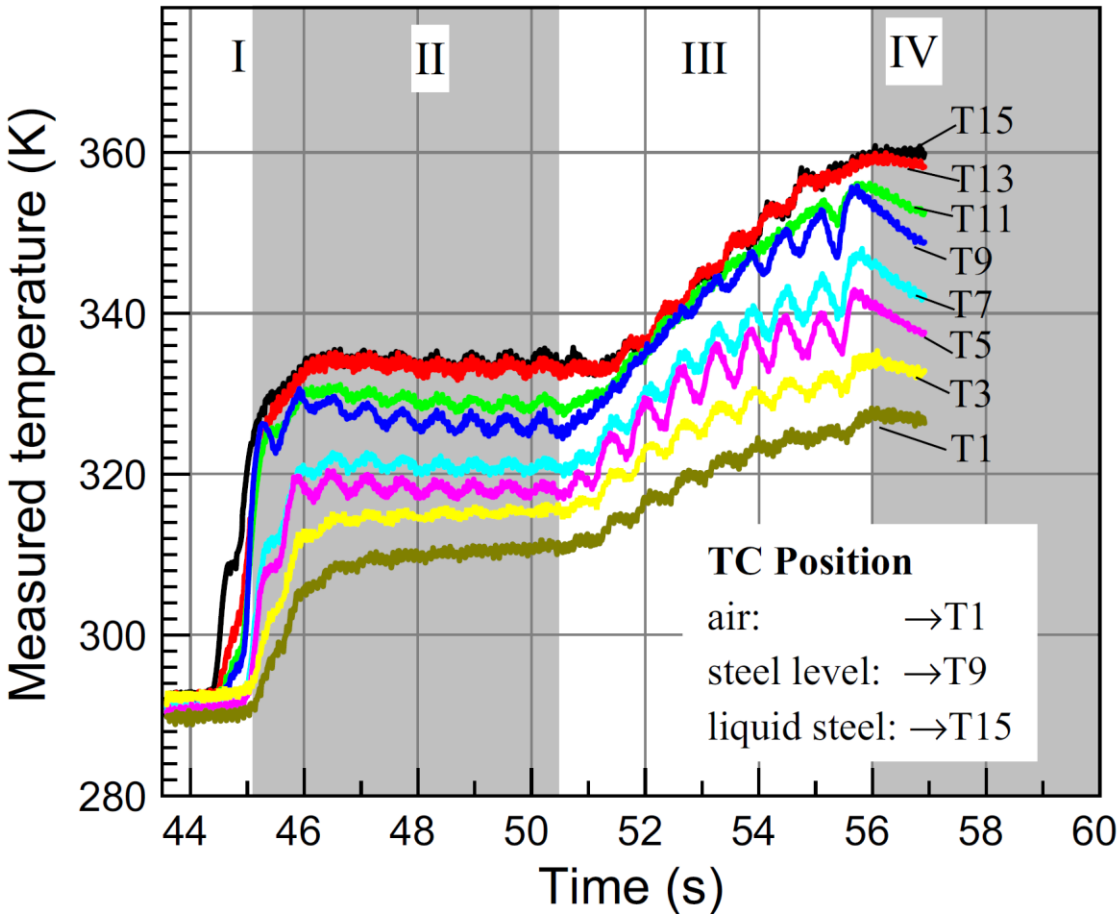

Figure 4.10: Measured temperature for the 1st column thermocouples during Zhang's experiments

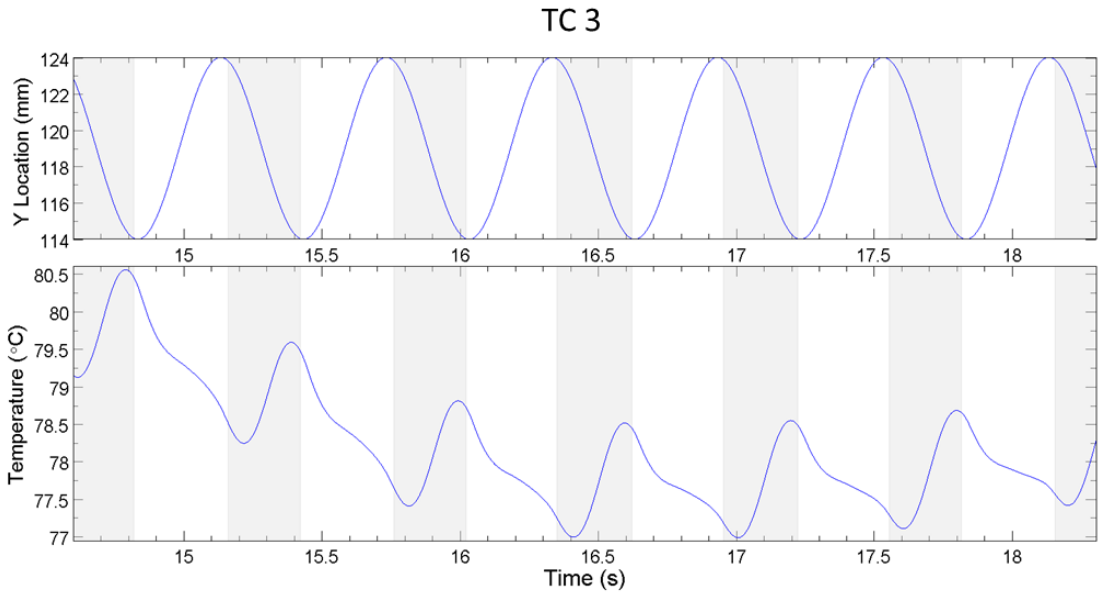

Figure 4.11: Transient temperature prediction with instantaneous vertical location at TC3 (hot) over 6 cycles

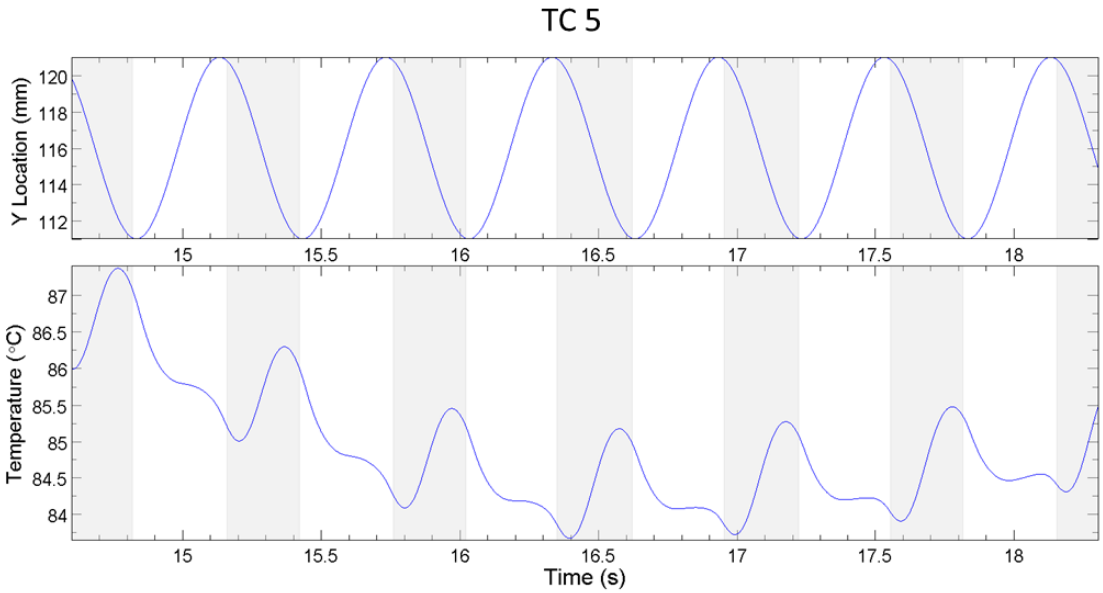

Figure 4.12: Transient temperature prediction with instantaneous vertical location at TC5 (hot) over 6 cycles

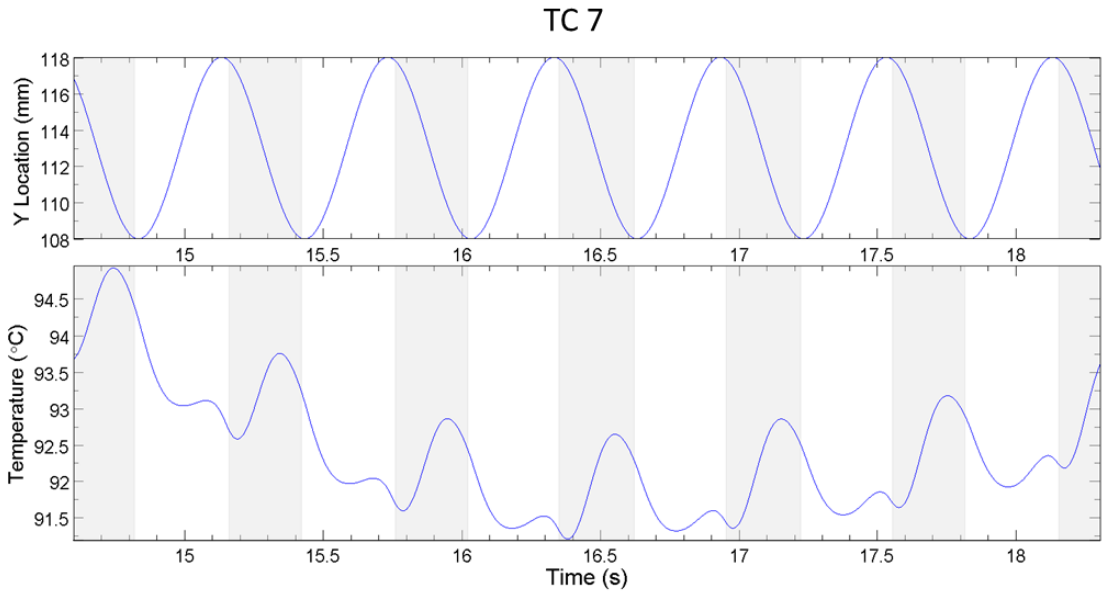

Figure 4.13: Transient temperature prediction with instantaneous vertical location at TC7 (hot) over 6 cycles

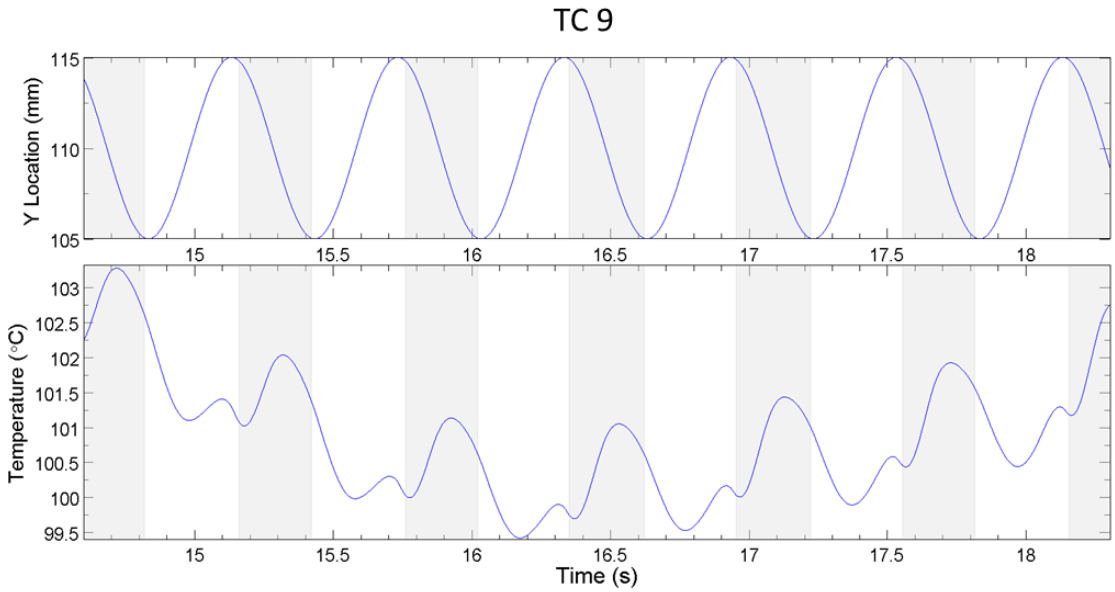

Figure 4.14: Transient temperature prediction with instantaneous vertical location at TC9 (hot) over 6 cycles

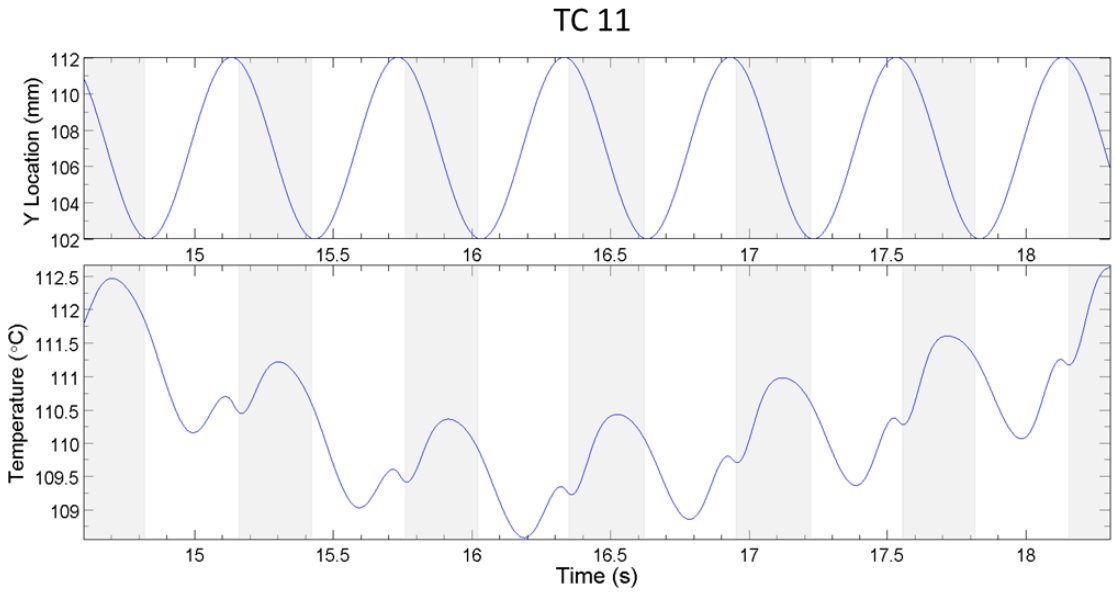

Figure 4.15: Transient temperature prediction with instantaneous vertical location at TC11 (hot) over 6 cycles

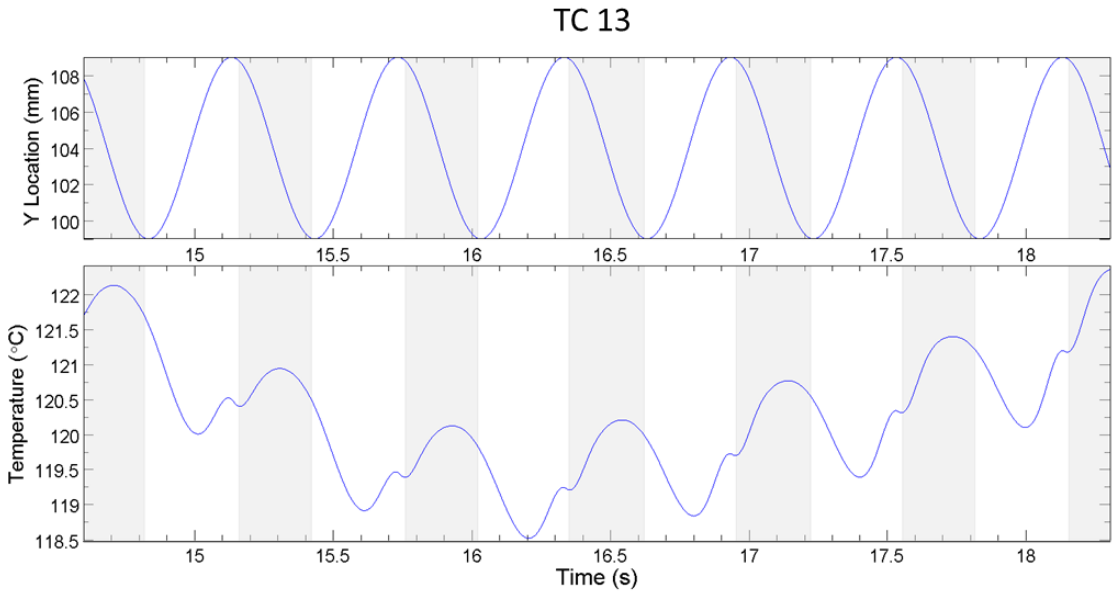

Figure 4.16: Transient temperature prediction with instantaneous vertical location at TC13 (hot) over 6 cycles

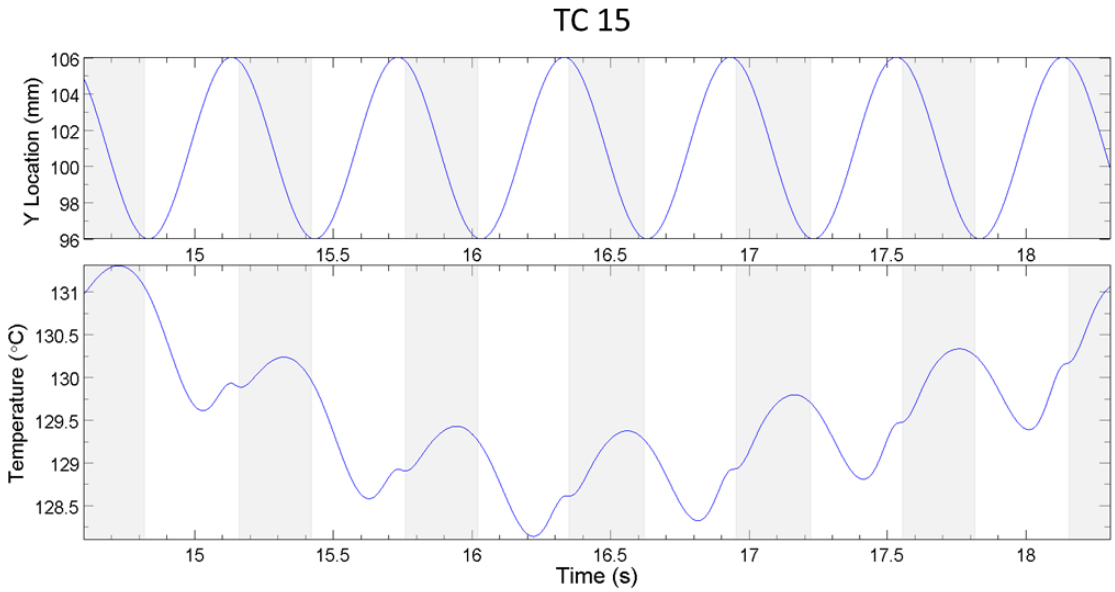

Figure 4.17: Transient temperature prediction with instantaneous vertical location at TC15 (hot) over 6 cycles

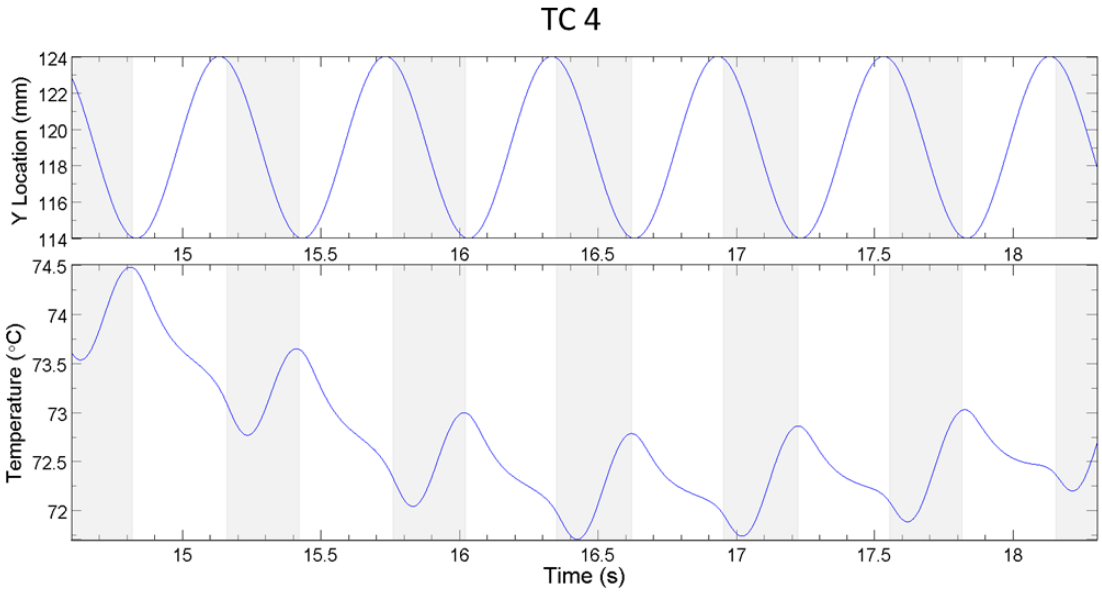

Figure 4.18: Transient temperature prediction with instantaneous vertical location at TC4 (cold) over 6 cycles

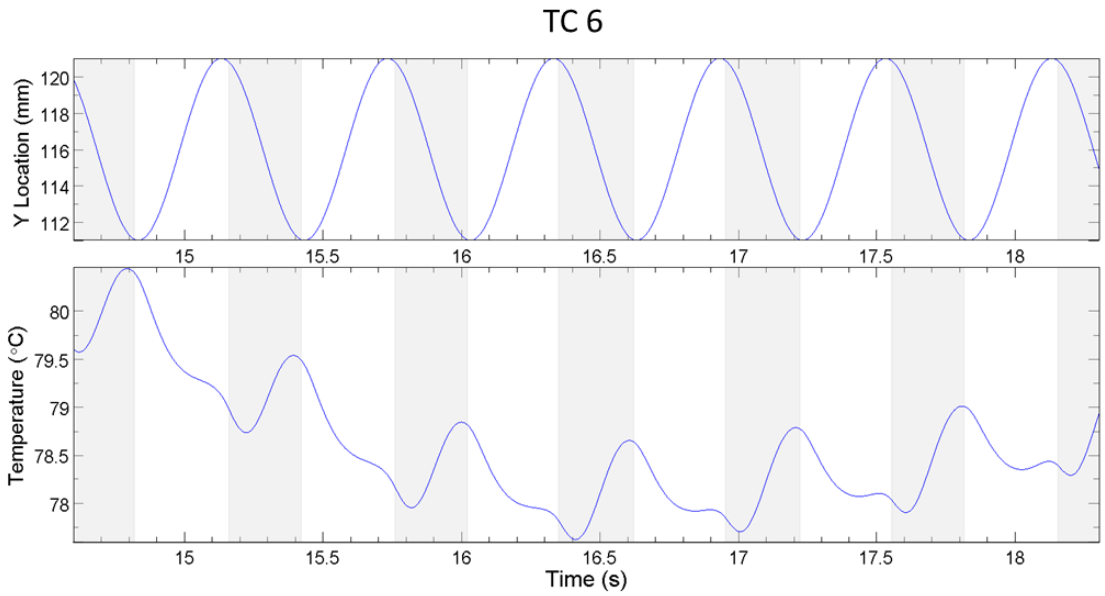

Figure 4.19: Transient temperature prediction with instantaneous vertical location at TC6 (cold) over 6 cycles

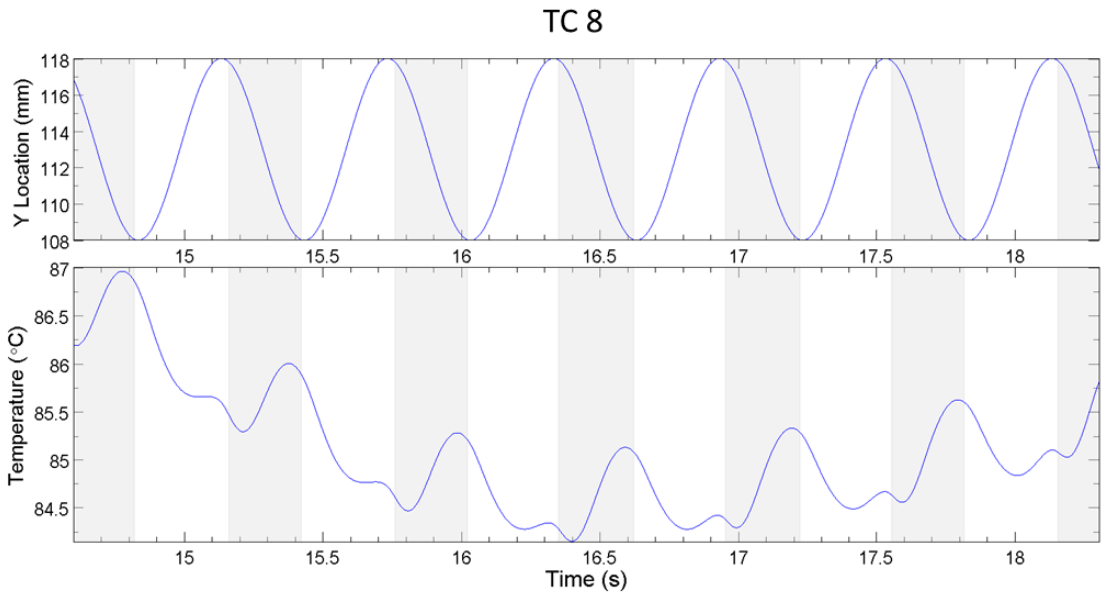

Figure 4.20: Transient temperature prediction with instantaneous vertical location at TC8 (cold) over 6 cycles

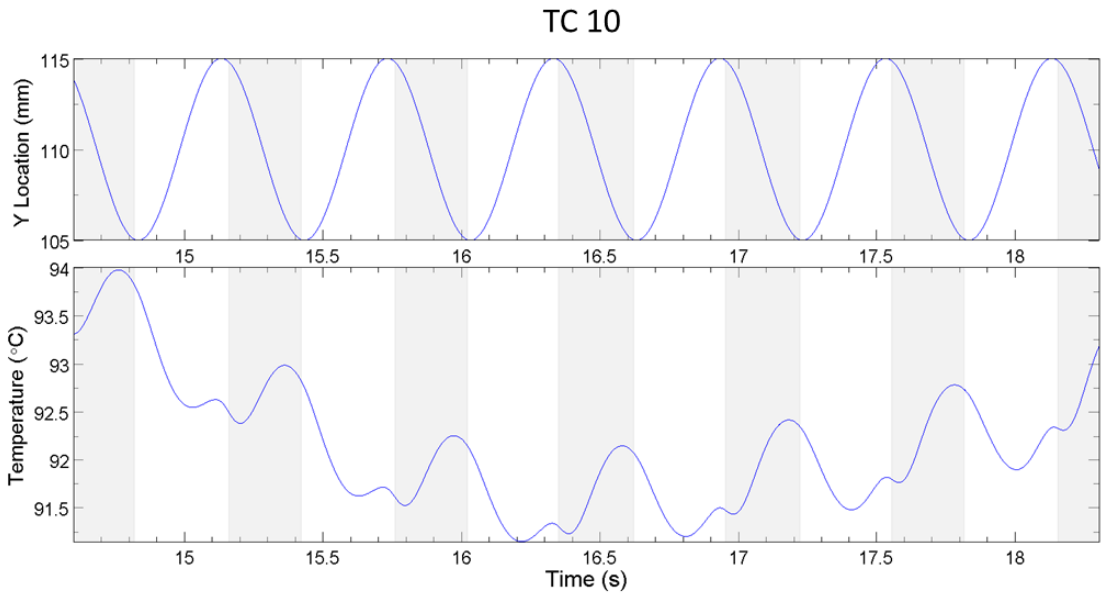

Figure 4.21: Transient temperature prediction with instantaneous vertical location at TC10 (cold) over 6 cycles

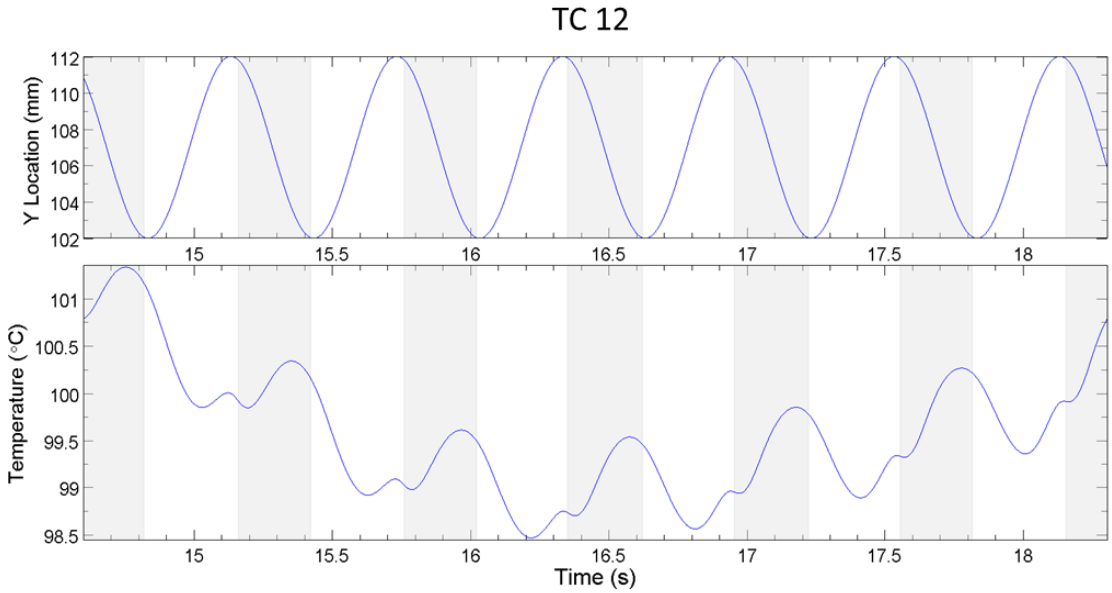

Figure 4.22: Transient temperature prediction with instantaneous vertical location at TC12 (cold) over 6 cycles

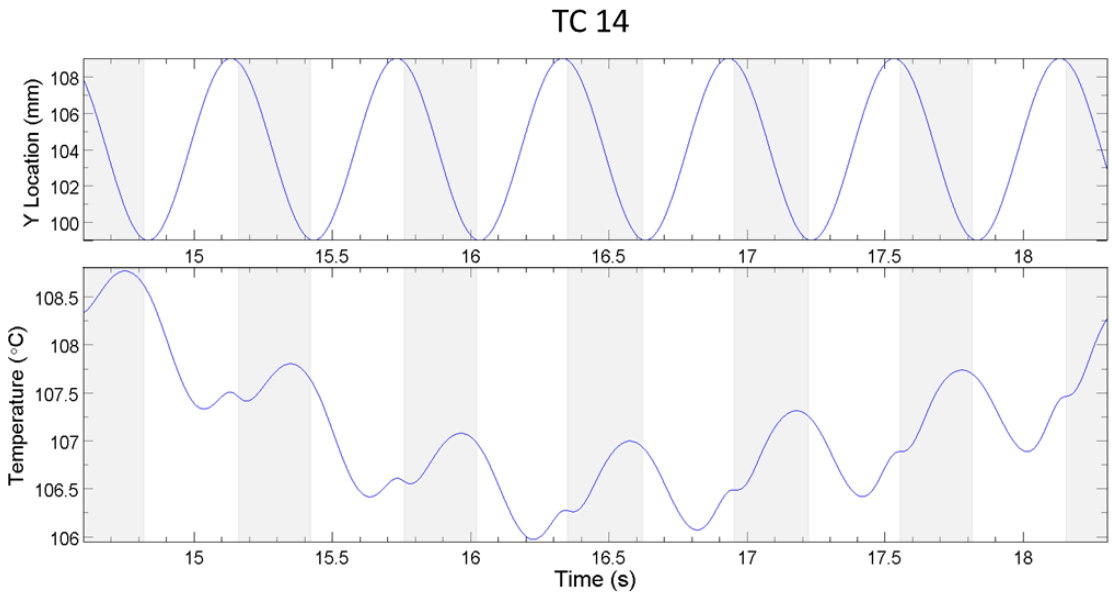

Figure 4.23: Transient temperature prediction with instantaneous vertical location at TC14 (cold) over 6 cycles

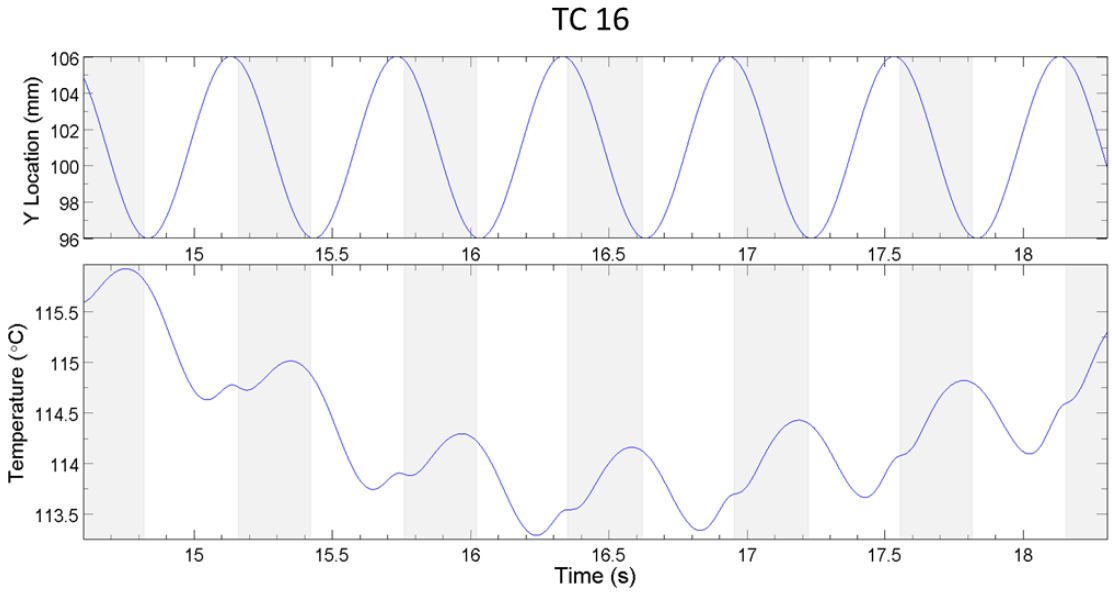

Figure 4.24: Transient temperature prediction with instantaneous vertical location at TC16 (cold) over 6 cycles

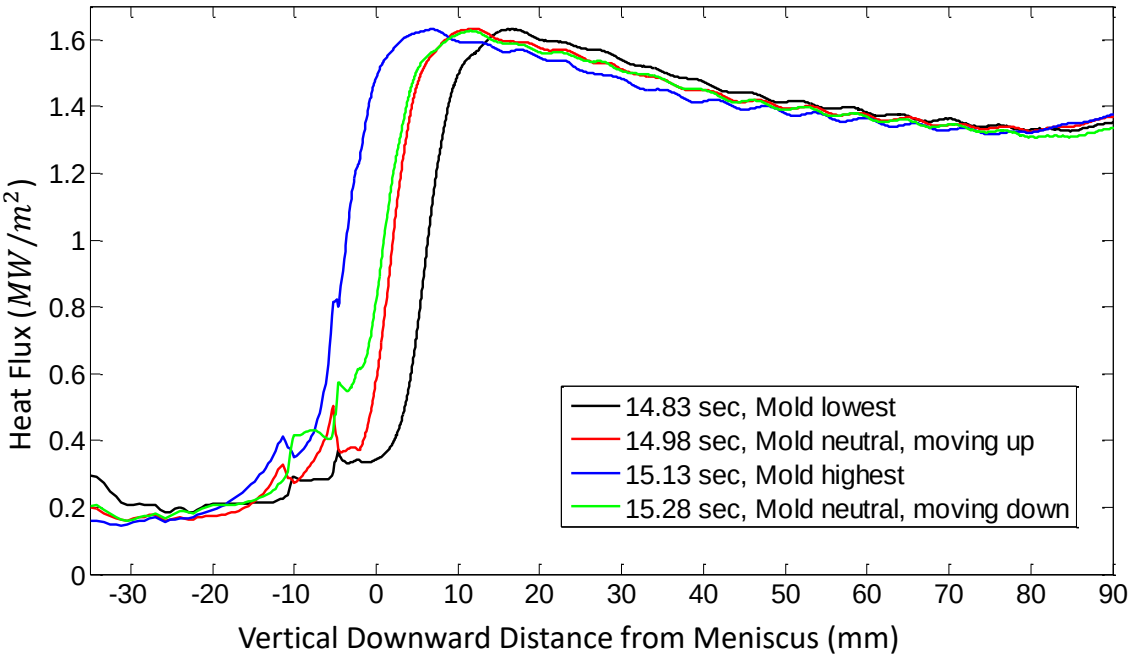

Figure 4.25: Predicted heat flux profile at mold hot face over an oscillation cycle

4.7 Tables

Table 4.1: Net slag consumption over 5 cycles

Cycle#	*1*	*2*	*3*	*4*	*5*	*Average*
Net consumption $(g/m \cdot s)$	*5.8*	*8.1*	*11.8*	*11.5*	*10.2*	*9.48*

CHAPTER 5: CONCLUSION

The current work presents a computational model to predict thermal-flow behavior of the steel, slag, and mold near the meniscus in a continuous-casting mold. This model is able to accurately predict transient evolution of the slag gap, solidifying steel shell strand profile, slag consumption, and oscillation mark shape, enabling better understanding of oscillation mark formation mechanisms. Model predictions match reasonably well with lab experiments, plant measurements and literature. The following conclusions can be drawn:

1. The slag and liquid-steel interface in the meniscus region follows the oscillating movement of the mold and slag rim. The meniscus bulges upwards during the positive strip time and is flattened downwards during the negative strip time.
2. Initial solidification of the shell is intermittent. New shell is formed during the positive strip time in an oscillation cycle, when liquid steel is brought close to mold. During the negative strip time, liquid steel is pushed down and held inside the shell strand, as it moves down the mold at the casting speed, while the shell only grows in thickness.
3. Hook type oscillation marks can be formed by liquid steel overflowing the shell tip during the positive strip time. A hook is formed by solidification of part of the meniscus at top of the previous shell tip. The interface between the newly formed shell caused by the overflow and this previous shell tip becomes the oscillation mark.
4. Overflow starts at the beginning of PST. Hence, the location of the root of a hook-type OM on a shell strand can be mapped in time to the start of PST.
5. Shell tip thickness is larger than that predicted by the square root law due to two dimensional cooling from both the mold and the slag layer, which freezes the meniscus region, and creates the hook.

6. Temperature inside the copper mold wall near the steel level increases during NST due to this part of mold getting closer to the hot meniscus. Another small temperature increase happens during the PST due to steel overflow of the solidified meniscus hook, which then brings the meniscus closer to the mold.

CHAPTER 6: REFERENCES

[1] Sengupta, J., and B. G. Thomas, "Visualization of Hook and Oscillation Mark Formation Mechanism in Ultra-Low Carbon Steel Slabs During Continuous Casting," JOMe, (Journal of Metals – electronic edition), December 2006

[2] Joydeep Sengupta, Brian G Thomas, Ho-Jung Shin, Go-Gi Lee and Seon-Hyo Kim, A New Mechanism of Hook Formation During Continuous Casting of Ultra-Low-Carbon Steel Slabs, Metall. Mater. Trans. A 2006, vol. 37, pp. 1597-1611.

[3] Haihui Zhang, Wanlin Wang, Fanjun Ma, and Lejn Zhou, Mold Simulator Study of the Initial Solidification of Molten Steel in Continuous Casting Mold. Part I: Experiment Process and Measurement, The Minerals, Metallurgical and Materials Transactions B, Volume 46b, October 2015—2361

[4] Ho-Jung Shin, S. H. Kim, B. G. Thomas, G. G. Lee, J. M. Park and J. Sengupta, Measurement and Prediction of Lubrication, Powder Consumption, and Oscillation Mark Profiles in Ultra-Low Carbon Steel Slabs, ISIJ Int. 2006, vol. 46, pp. 1635-1644.

[5] K Tsutsumi, H Murakami, SI Nishioka, M Tada, M Nakada and M Komatsu, Estimation of Mold Powder Consumption in Continuous Casting, Trans. Iron Steel Inst. Jpn. 1998, vol. 84, pp. 617-624.

[6] Mikio Suzuki, Makoto Suzuki and Masayuki Nakada, Perspectives of Research on High- Speed Conventional Slabcontinuous Casting of Carbon Steels, ISIJ Int. 2001, vol. 41, pp. 670-682.

[7] M. Kawamoto, T. Murakami, M. Hanao, H. Kikuchi and T. Watanabe, Mould Powder Consumption of Continuous Casting Operations, Ironmaking Steelmaking 2002, vol. 29, pp. 199-202.

[8] M.M. Wolf, Mold Oscillation Guidelines, In 1991 Steelmaking Conference, (Washington, D.C., USA, 1991), pp. 51-71.

[9] Wolf: PTD Cong. Proc., Nashville, TN, ISSS, Warrendale, PA, 1995, pp 99-117

[10] A.W. Cramb and F.J. Mannion, Measurement of Meniscus Marks at Bethlehem Steel's Burns Harbor Slab Caster., *Steelmaking Conference Proceedings*, p 349-359, 1985, Warrendale, PA, US

[11] M. Bobadilla, J. M. Jolivet, J. Y. Lamant and M. Larrecq, Continuous Casting of Steel: A Close Connection between Solidification Studies and Industrial Process Development, Mater. Sci. Eng., Proc. Conf. 1993, vol. 173, pp. 275-285.

[12] T Darle, A Mouchette, M Roscini, M Nadif and D Salvadori, Hydraulic Oscillation of the CC Slab Mold at Sollac Florange: First Industrial Results, Future Developments, In 76 the Steelmaking Conf., (1993), pp. 209-218.

[13] J.J. Bikerman: Physical Surfaces, Academic Press, New York, 1970, pp. 11–12.

[14]A Badri, TT Natarajan, CC Snyder, KD Powers, FJ Mannion, M Byrne and AW Cramb, A Mold Simulator for Continuous Casting of Steel: Part Ii. The Formation of Oscillation Marks 92 During the Continuous Casting of Low Carbon Steel, Metall. Mater. Trans. B 2005, vol. 36, pp. 373-383.

[15]A Badri, TT Natarajan, CC Snyder, KD Powers, FJ Mannion and AW Cramb, A Mold Simulator for the Continuous Casting of Steel: Part I. The Development of a Simulator, Metall. Mater. Trans. B 2005, vol. 36, pp. 355-371.

[16]E. Takeuchi and J.K. Brimacombe, The Formation of Oscillation Marks in the Continuous Casting of Steel Slabs, Metall. Mater. Trans. B 1984, vol. 15B, pp. 493-509.

[17]Quan Yuan, B. G. Thomas, and S. P. Vanka, Turbulent Flow and Particle Motion in Continuous Slab-Casting Molds, ISSTech 2003 (Conf. Proc.), Indianapolis, IN, USA, Apr. 27-30, 2003, ISS-AIME, Warrendale, PA, 2003, pp. 913-927.

[18]Chaudhary, R., C. Ji, S.P. Vanka, and B.G. Thomas “Transient Turbulent Flow in a Liquid-Metal Model of Continuous Casting, Including Comparison of Six Different Methods”, Metallurgical and Materials Trans. B, in press, 2011.

[19]Liu, Rui, Brian G. Thomas, Bruce Forman and Hongbin Yin, "Transient Turbulent Flow Simulation with Water Model Validation and Application to Slide Gate Dithering," AISTech 2012, (Atlanta, GA, May 7-9, 2012), 2012.

[20] Cho, Seong-Mook, Kim, Seon-Hyo, and Brian G. Thomas, “Transient Fluid Flow during Steady Continuous Casting of Steel Slabs, Part I: Measurements and Modeling of Two-phase Flow", ISIJ International, Vol. 54, No. 4, (April), pp. 845-854, 2014.

[21] R. M. McDavid and B. G. Thomas, Flow and Thermal Behavior of the Top Surface Flux/Powder Layers in Continuous Casting Molds, Metallurgical and Materials Transactions BProcess Metallurgy and Materials Processing Science 1996, vol. 27, pp. 672-685.

[22] Meng, Y. and B. G. Thomas, “Heat-Transfer and Solidification Model of Continuous Slab Casting: CON1D,” Metallurgical & Materials Transactions B, 34B:5, 685-705, 2003.

[23] Meng, Y. and B. G. Thomas, “Modeling Transient Slag-Layer Phenomena in the Shell/Mold Gap in Continuous Casting of Steel,” Metallurgical & Materials Transactions B, 34B:5, 707-725, 2003.

[24] Meng, Y. and B. G. Thomas, “Simulation of Microstructure and Behavior of Interfacial Mold Slag Layers in Continuous Casting of Steel,” ISIJ International, 46:5, 660-669, May 2006.

[25] Lance C. Hibbelera, Melody M. Chin Seeb, Junya Iwasakic, Kenneth E. Swartza, Ronald J. O’Malleyd, Brian G. Thomas, “A reduced-order model of mould heat transfer in the continuous casting of steel” Applied Mathematical Modelling, Volume 40, Issues 19–20, October 2016, Pages 8530–8551

[26]Xin, Xie. "Mathematical Modeling of Heat Transfer in Mold Copper Coupled with Cooling Water During the Slab Continuous Casting Process." Metallurgical and Materials Transactions B 45.6 (2014):2442-52. Web.

[27]Sengupta, J., C. Ojeda and B. G. Thomas, “Thermal-Mechanical Behaviour during Initial Solidification in Continuous Casting: Steel Grade Effects”, Int. J. Cast Metals Research, 22:1-4, 8-14, 2009.

[28]Li, C. and B. G. Thomas, “Thermo-Mechanical Finite-Element Model of Shell Behavior in Continuous Casting of Steel,” Metallurgical and Materials Transactions B, 35B:6, 1151-1172, 2004.

[29]Kozlowski, P. F., B. G. Thomas, J. Azzi, and H. Wang, "Simple Constitutive Equations for Steel at High Temperature," Metallurgical Transactions A, 23A:3, 903-918, 1992.

[30]Thomas, B. G. and H. Zhu, "Thermal Distortion of Solidifying Shell in Continuous Casting of Steel, "Solidification Science and Processing, I. Ohnaka and D. M. Stefanescu, eds., Japan Inst. Metals 117th Fall Annual Meeting, Honolulu, HI, Dec. 13-15, 1995; The Minerals, Metals, and Materials Society, Warrendale, PA, 197-208, 1996.

[31]H Steinruck and Christian Rudischer, Numerical Investigation of the Entrainment of Flux into the Lubrication Gap in Continuous Casting of Steel, In Fifth World Congress on Computational Mechanics, (2002).

[32]Claudio Ojeda, Joydeep Sengupta, Brian G. Thomas, Jon Barco and Jose Luis Arana, Mathematical Modeling of Thermal-Fluid Flow in the Meniscus Region During an Oscillation 91 Cycle, In AISTech 2006 - Iron and Steel Technology Conference, May 1 - 4 2006, (Association for Iron and Steel Technology, AISTECH: Cleveland, OH, United states, 2006), pp. 1017-1028.

[33]Claudio Ojeda, Brian G. Thomas, Jon Barco and Jose Luis Arana, Model of Thermal-Fluid Flow in the Meniscus Region During an Oscillation Cycle, In AISTech 2007 - Iron and Steel Technology Conference, May 7 - 10 2007, (Association for Iron and Steel Technology, AISTECH: Indianapolis, IN, United states, 2007), pp. 269-283.

[34]ASM Jonayat and Brian G. Thomas, "Transient Thermo-Fluid Model of Meniscus Behavior and Slag Consumption in Steel Continuous Casting", Metallurgical and Materials Transactions B, 45: 5, (Oct.), pp. 1842-1864, 2014. DOI: 10.1007/s11663-014-0097-9.

[35]C. W. Hirt and B. D. Nichols, Volume of Fluid (Vof) Method for the Dynamics of Free Boundaries, J. Comput. Phys. 1981, vol. 39, pp. 201-225.

[36]T Tanaka and K Takatani, Hydrodynamics of Molten Powder in the Vicinity of Meniscus in Continuous Casting, CAMP-ISIJ 1989.

[37]Hong Sha, Ralf Diedrichs and Klaus Schwerdtfeger, Dynamic Behavior of a Liquid/Liquid Interface at an Oscillating Wall, Metall. Mater. Trans. B 1996, vol. 27, pp. 305-314.

[38]Pavel E. Ramirez Lopez, Kenneth C. Mills, Peter D. Lee and Begona Santillana, A Unified Mechanism for the Formation of Oscillation Marks, Metall. Mater. Trans. B 2012, vol. 43, pp. 109-122.

[39]Pavel E. Ramirez-Lopez, Peter D. Lee and Kenneth C. Mills, Explicit Modelling of Slag Infiltration and Shell Formation During Mould Oscillation in Continuous Casting, ISIJ Int. 2010, vol. 50, pp. 425-434.

[40]Pavel E. Ramirez Lopez, Peter D. Lee, Kenneth C. Mills and Begona Santillana, A New Approach for Modelling Slag Infiltration and Solidification in a Continuous Casting Mould, ISIJ International, Vol. 50 (2010), No. 12, pp. 1797–1804

[41]V. R. Voller and C. Prakash, A Fixed Grid Numerical Modelling Methodology for Convection-Diffusion Mushy Region Phase-Change Problems, Int. J. Heat Mass Transfer 1987, vol. 30, pp. 1709-1719.

[42]M. Hanao and M. Kawamoto: ISIJ Int., 48 (2008), 180.

[43]P. Lundkvist, B. Bergquist, Experimental study of oscillation mark depth in continuous casting of steel, Ironmaking & Steelmaking 2014, 41:4, 304-309

[44]J. U. Brackbill, D. B. Kothe and C. Zemach, A Continuum Method for Modeling Surface-Tension, J. Comput. Phys. 1992, vol. 100, pp. 335-354.

[45]M. Ishii: Thermo-Fluid Dynamic Theory of Two-Phase Flow. (Eyrolles, 1975).

[46]F. R. Menter, 2-Equation Eddy-Viscosity Turbulence Models for Engineering Applications, AIAA J. 1994, vol. 32, pp. 1598-1605.

[47]FR Menter, M Kuntz and R Langtry, Ten Years of Industrial Experience with the SST Turbulence Model, Turbulence, heat and mass transfer 2003, vol. 4, pp. 625-632.

[48]ANSYS Fluent. 13.0, Canonsburg, PA, 2013.

[49]Ya Meng and Brian G Thomas, Heat-Transfer and Solidification Model of Continuous Slab Casting: Con1d, Metall. Mater. Trans. B 2003, vol. 34, pp. 685-705.

[50]C.A. Sleicher and M.W. Rouse, A Convenient Correlation for Heat Transfer to Constant and Variable Property Fluids in Turbulent Pipe Flow, Int. J. Heat Mass Transfer 1975, vol. 18, pp. 677-683.

[51]T. Kawawa: Tekko-no-Gyoko (Solidification of Steel), Solidification Communications of ISIJ, ISIJ, Tokyo, 1977, Appendix 13.

[52]B.G. Thomas and J.T. Parkman: Thermec '97, Int. Conf. on Thermomechanical Processing of Steel and Other Materials, Wollongong, Australia, 1997, TMS, Warrendale, PA, 1997, vol. II, pp. 2279-85.

[53]Y. Nakamura and H. Esaka: Tetsu-to-Hagane´, 1981, vol. 67, p. S140.

[54]Tekko-no-Gyoko (Solidification of Steel), supplement, Solidification Communications of ISIJ, ISIJ, Tokyo, 1977, pp. S32-S50.

[55]Metals Handbook, 8th ed., T. Lyman, H.E. Boyer, W.J. Carnes, and M.W. Chevalier, eds., ASM, Metal Park, OH, 1973.

[56]Tekko-Binran (Handbook for Steel), 3rd ed., ISIJ, Maruzen, Tokyo, 1981, vol. 1, pp. 193-94.

[57]Sengupta, J., H.-J. Shin, B. G. Thomas, and S.-H. Kim, "Micrograph Evidence of Meniscus Solidification and Sub-Surface Microstructure Evolution in Continuous-Cast Ultra-Low Carbon Steels," Acta Materialia, 54:4, 1165-1173, February 2006

APPENDIX: Model Set-Up in FLUENT[48]

1. Import mesh for both mold and fluid domain from Gambit .msh file, scale the mesh down if mm is used in Gambit for mesh creation (Fluent uses SI units by default).
2. Set up material properties, boundary conditions and calculation parameters as described in previous chapters.
3. Standard initialize the model with the UDF "interface" hooked. This step is to prescribe the Bikerman phase interface shape.
4. Perform a flow only transient simulation with no mold oscillation, no steel inflow. This is to smooth out the small edges on the bikerman interface we just created by UDF.

   Detail:

   - Go to model, Turn off solidification, set viscous to laminar
   - Go to solution method, select equations, uncheck heat transfer
   - Change slag viscosity to constant = 0.1
   - Run transient until the interface is smooth, should only take several minutes of wall clock time
5. After establishing the slag and steel interface, perform a thermal only steady state simulation to create shell profile and initialize temperature field.

   Detail:

   - Standard initialize the velocity only (use the patch option, v=0) (this is to clean up the velocity field, because any velocity will mess up a steady state simulation by heat advection)
   - Select steady state

- Go to model, turn on solidification, make sure turbulence is turn off (laminar)
- Go to solution method, select equations, check heat transfer, uncheck flow, uncheck VOF
- Make sure the “fix-temp-initial” is hooked and all other thermal boundary is properly set
- Run steady state until convergence

6. After establishing the slag temperature field and steel shell profile, a full transient simulation should be carried out without the mold oscillation. This is to establish the liquid steel flow field as well as the temperature field.

   Detail:

   - Unhook “fix-temp-initial”, hook “fix-steel-temp”, hook “fix-shell-vel”
   - Select transient, turn on turbulence
   - Check all equations in the solution method
   - Restore correct slag viscosity
   - Standard initialize turbulence k and w to 1e-5 (patching)
   - Run transient until flow field reaches steady state

7. Include mold oscillation in the mold zone condition, and run transient. It is advised to use very small time steps when starting up a transient simulation, or after some major parameter change (sometimes 1e-9s is necessary). After it converges better (within 5 iterations), gradually increase the time step to where appropriate (for this model, 1e-5s or 2e-5s).